Pacific Northwest
NATIONAL LABORATORY

PNNL-36747

Results of Post-Process NDE Using Advanced Techniques on AM Parts

M2CT-24PN1305061

September 2024

Pacific Northwest National Laboratory
Robert O. Montgomery
Chris Hutchinson
Nicholas A. Conway
Morris S. Good
Richard E. Jacob
Isabella Van Rooyen

Idaho National Laboratory
William C. Chuirazzi
Zilong Hua
Chuting Tsai
Brian Newell

U.S. DEPARTMENT OF ENERGY

Prepared for the U.S. Department of Energy
under Contract DE-AC05-76RL01830

DISCLAIMER

PACIFIC NORTHWEST NATIONAL LABORATORY
operated by
BATTELLE
for the
UNITED STATES DEPARTMENT OF ENERGY
under Contract DE-AC05-76RL01830

Printed in the United States of America

Available to DOE and DOE contractors from
the Office of Scientific and Technical Information,
P.O. Box 62, Oak Ridge, TN 37831-0062
www.osti.gov
ph: (865) 576-8401
fox: (865) 576-5728
email: reports@osti.gov

Available to the public from the National Technical Information Service
5301 Shawnee Rd., Alexandria, VA 22312
ph: (800) 553-NTIS (6847)
or (703) 605-6000
email: info@ntis.gov
Online ordering: http://www.ntis.gov

PNNL-36747

Results of Post-Process NDE Using Advanced Techniques on AM Parts

M2CT-24PN1305061

September 2024

Pacific Northwest National Laboratory
Robert O. Montgomery
Chris Hutchinson
Nicholas A. Conway
Morris S. Good
Richard E. Jacob
Isabella Van Rooyen

Idaho National Laboratory
William C. Chuirazzi
Zilong Hua
Chuting Tsai
Brian Newell

Prepared for
the U.S. Department of Energy
under Contract DE-AC05-76RL01830

Pacific Northwest National Laboratory
Richland, Washington 99354

Page Intentionally
Left Blank

Summary

The Advanced Materials and Manufacturing Technology (AMMT) program is accelerating the development, qualification, demonstration, and deployment of advanced materials and manufacturing technologies for advanced and current nuclear reactor systems (Li et. al., 2022). The development and use of post-process nondestructive examination (NDE) methods is critical to the qualification and verification of materials and components from advanced manufacturing (AM) processes, such as Laser Powder Bed Fusion (LPBF) or Directed Energy Deposition (DED) technologies. Overcoming the unique challenges of AM components and materials (e.g surface roughness, geometric complexity, microstructural features, and defect morphology) to provide reliable and high resolution NDE is the primary objective of the post-process NDE activities within the AMMT program. The ability to perform reliable and accurate NDE throughout a component lifetime will further drive the adoption of AM fabricated components for safety critical applications.

The post-process NDE activities in the AMMT consists of a multi-laboratory collaboration that has been working over the last two years to perform and evaluate different modalities of NDE to characterize the material characteristics of coupons and components fabricated using AM processes. This report provides an overview of the fiscal year (FY) 2024 activities to apply advanced NDE methods to materials and components produced using LPBF and DED and assess the challenges of examining these materials to identify defects and microstructure variations.

The post-process NDE techniques used this fiscal year included a variety of methods that span the length scale from angstroms to millimeters. Such techniques were used to evaluate microstructural features such atomic vacancies, measure the residual stress from changes in atomic lattice spacing, imaging of porosity, and measurement of elastic properties in a variety of materials coupons fabricated with LPBF or DED processes. Table 1 provides a summary of the post-process NDE techniques included in the FY24 work scope.

Table 1. Post-Process NDE Techniques Evaluated in FY24

NDE Technique	Parameter of Interest	Considerations
X-Ray Computed Tomography (XCT)	Porosity and Defects	Sample size and scan times
X-Ray Diffraction (XRD)	Residual Stress	Sample size, Lab scale
Neutron Computed Tomography (nCT)	Porosity and Defects	Neutron source availability
Neutron Diffraction	Residual Stress	Neutron source availability
Lock-in Thermography (LIT)	Thermal Diffusivity	Surface conditions
Positron Annihilation Spectroscopy (PAS)	Atomic vacancy distributions	Lab scale, sample size
Resonance Ultrasound Spectroscopy (RUS)	Elastic Properties	Samples size
Scanning Acoustic Microscopy (SAM)	Porosity and Defects	Sample size
Linear Pulse Echo Ultrasonic Testing (UT)	Elastic Properties, Defects	Surface conditions
Reflected Ultrasonic Amplitude Spectrum Analysis (RUASA)	Geometric Variability and Defects	Surface conditions

Relevant materials produced using AM processes included coupons of austenitic stainless steel (SS) Alloy 709 and ferritic/martensitic SS Grade 92 produced by LPBF processes and SS grade 316L (SS316L) produced by DED processes. Additionally, a SS316L cylindrical component fabricated with laser powder DED processes was evaluated in the as-fabricated condition and following different levels of surface machining operations.

Through the application of advanced NDE methods, material anisotropy effects in ultrasonic and mechanical properties were identified, imaging and sizing of material defects were performed, and several material and component challenges unique to AM processes were recognized, such as variable residual stress in material fabricated using DED.

An important achievement this year was the multi-modal collaboration through complimentary examinations of DED 316L coupons by X-ray computed tomography (XCT), LIT and UT approaches. Preliminary ultrasonic imaging and RUS analyses generated characterization results that were consistent with the XCT images and LIT evaluations obtained for the two DED 316L material coupons. The UT techniques were able to locate the porosity/defects within the coupons and provide estimates of the impact of these defects on the material elastic mechanical properties. This exercise provides an example of how complimentary examination techniques can facilitate the scale up of methods to qualify full size component inspections.

A critical step in correlating NDE modalities will be coordinating data from in-situ monitoring, XCT and nCT, ultrasonic methods, and destructive examinations to establish material properties and the presence and distribution of defects. These data fusion efforts will make use of consistent spatial registration techniques, correlation of data signals, and data analytics to develop the relationships between the different NDE methods.

As the NDE work within that AMMT program has progressed, a new NDE paradigm to qualify full size components from AM processes is evolving that consists of printing witness coupons during a component build that can be inspected using destructive and nondestructive characterization methods to provide information on the material conditions produced by a build. This information is then used to confirm the final build state of the component using fast and inexpensive validated volumetric inspection methods such as ultrasonic or eddy current techniques in key locations or subcomponent regions. These locations could be determined by probabilistic risk assessments performed to identify regions in the component susceptible to potential flaw nucleation and growth. Development and confirmation of this approach should be a major focus in future research and development (R&D) efforts.

Acknowledgments

The research presented in this report was supported by the AMMT program of the U.S. Department of Energy (DOE) Office of Nuclear Energy. Pacific Northwest National Laboratory (PNNL) is a multi-program national laboratory operated for the U.S. DOE by Battelle Memorial Institute under Contract No. DE-AC05-76RL01830.

The authors would like to acknowledge the contributions of the LBPF team at Argonne National Laboratory (ANL) managed by Xuan Zhang and her collaborator Srinivas Aditya Mantri in providing the Alloy 709 and Grade 92 material coupons. The contributions from the DED Team at Idaho National Laboratory (INL) are gratefully acknowledged for the generation of the DED 316L material coupons. The DED 316L cylinder examined in this report was fabricated by AMMT work package CT-24PN130405 directed by Isabella Van Rooyen at PNNL. The authors are appreciative to Isabella Van Rooyen and Mohan Nartu from PNNL for supplying and assisting in the efforts to perform nondestructive examinations on the cylinder.

Acronyms and Abbreviations

AM	advanced manufacturing
AMMT	Advanced Materials and Manufacturing Technologies
ANL	Argonne National Laboratory
ASME	American Society of Mechanical Engineers
CT	computed tomography
DED	directed energy deposition
DMA	degradation mechanisms assessment
FFT	fast fourier transform
FGM	functionally graded material
FY	fiscal year
INL	Idaho National Laboratory
LIT	lock-in infrared thermography
LPBF	laser powder bed fusion
MANDE	monitoring and nondestructive examination
MLIT	multi-point lock-in infrared thermography
nCT	neutron computed tomography
NDE	nondestructive evaluation
ORNL	Oak Ridge National Laboratory
PAS	positron annihilation spectroscopy
PNNL	Pacific Northwest National Laboratory
PTR	photothermal radiometry
R&D	research and development
RIM	reliability and integrity management
RUS	resonant ultrasound spectroscopy
SNR	Signal-to-Noise Ratio
SS	stainless steel
SS316L	stainless steel grade 316L
SSCs	structures, systems, and components
ToF	time of flight
UT	ultrasonic testing
XCT	X-ray computed tomography
XRD	X-ray diffraction

Contents

Figures

Tables

1.0 Introduction

The purpose of this report is to provide an overview of the fiscal year (FY) 2024 activities to apply advanced nondestructive examination (NDE) methods to materials and components produced using advanced manufacturing (AM) processes such as Laser Powder Bed Fusion (LPBF) and Directed Energy Deposition (DED) and assess the challenges of examining these materials to identify defects and microstructure variations. This work was performed as part of the U.S. Department of Energy's Office of Nuclear Energy Advanced Materials and Manufacturing Technologies (AMMT) Program. The primary mission of the AMMT program is to develop advanced materials and manufacturing technologies that enable both the current fleet and the next generation of advanced nuclear reactors to operate safely and economically, and to maintain U.S. leadership in technology development for nuclear energy systems (Li et. al., 2022).

1.1 Post-Process NDE for Advanced Materials and Manufacturing Technologies (AMMT)

The AMMT program is accelerating the development, qualification, demonstration, and deployment of advanced materials and manufacturing technologies for advanced and current nuclear reactor systems (Li et. al., 2022). The development and use of post-process NDE methods is critical to the qualification and verification of materials and components from AM processes. Overcoming the challenges of the unique characteristics of AM components and materials (e.g surface roughness, geometric complexity, microstructural features, and defect morphology) to provide reliable and high resolution NDE is the primary focus of the AMMT program. By developing a post-process NDE methodology for safety critical components fabricated with AM processes, the AMMT program is addressing an important hurdle to the industry and regulatory adoption of these advanced fabrication techniques.

The AMMT post-process NDE effort encompasses a variety of methods that span the range from high resolution X-ray computed tomography (CT) and neutron diffraction to resonance ultrasound spectroscopy (RUS) to ultrasonic pulse-echo methods (Montgomery et. al., 2023a, Chuirazzi et. al., 2023). The objectives of these NDE methods are to identify the presence of porosity and internal defects, characterize the microstructure, assess the mechanical properties, and measure geometric conformity in the post-build condition. Combined with the in-situ monitoring data obtained during the build process, the use of post-process NDE will be able to further demonstrate the component conformance to material and geometric requirements.

The post-process NDE activities within the AMMT program are working to develop the capabilities to characterize the microstructure and defect morphologies across the different length and resolution scales present within AM materials and components. The activities are utilizing data from in-situ monitoring, X-ray CT (XCT) and neutron CT (nCT), ultrasonic methods, and destructive examinations to establish material properties and the presence and distribution of defects. As shown in Figure 1, the fusion of this data will require a well-defined set of AM process parameters, use of consistent spatial registration techniques, correlation of data signals, and data analytics to develop the relationships between different NDE methods. The development and utilization of this approach will establish a qualification process for AM components that can be scaled to full size components and can be used to inform the approaches necessary to conduct future in-service inspections.

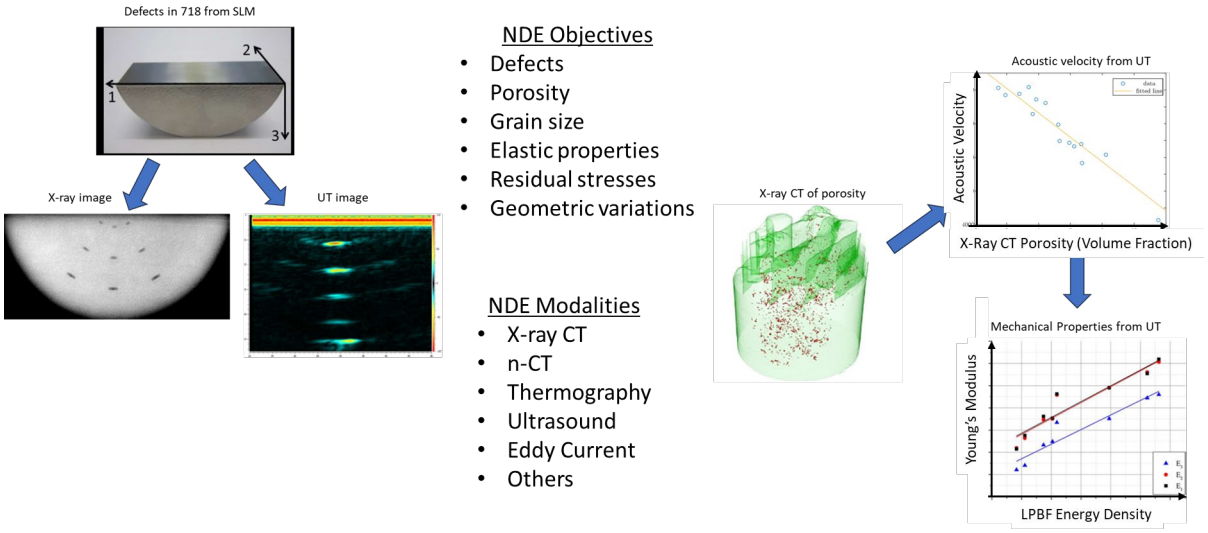

Figure 1. Schematic of NDE modalities and objectives for material and manufacturing process qualification within the DOE-NE AMMT Program

1.2 NDE Needs for Advanced Reactor Applications

AM methods such as LPBF and DED targeted for fabrication of advanced reactor components produce internal stresses, surface conditions, microstructural features, and defect morphologies that are significantly different than those from traditional fabrication processes such as forging, machining, and welding. Therefore, the NDE methods and techniques used to identify critical defects—and determine the influence of the microstructural morphologies on inspectability—are not well defined and must be tailored specifically for AM components. In 2023, America Makes and ANSI issued an update to the Standardization Roadmap for Additive Manufacturing which includes a gap assessment and priority areas of research and development (R&D) needs for industrialization of AM components and materials (AMSC 2023). Twelve of the 13 NDE gaps were ranked high or medium priority and were recognized as important for safety-critical components fabricated using AM processes. These gaps identify significant research needs for both post-process and in-service NDE. These needs include both pre-service and in-service identification of flaw types, sizes, and distributions, determination of the impact of microstructure on volumetric inspection techniques (e.g. anisotropy and attenuation), compensation for post-fabrication surface conditions, and development of acceptance criteria. As identified in the AMSC Roadmap, the amount of NDE research required for AM is formidable and requires immediate attention to keep up with the pace of rapid advancement in AM. It is important to understand that this research is not simply about applying existing NDE methods to new builds, but it involves developing novel NDE techniques that can address the unique problems that AM fabricated components pose.

CT inspection methods are the current gold standard for post-process inspection of small to moderately sized AM parts, especially from nonmetallic materials. These methods produce 3D images with high-resolution and high contrast. However, XCT inspections are often limited by component size, thickness, and composition, while neutron inspection methods are limited by the general lack of neutron source availability. The CT methods are not useful for characterizing microstructure and material properties (such as elastic moduli), and tightly closed cracks may not be detectable in CT images. Furthermore, the lack of portability makes CT methods inappropriate for in-service inspections, where a part or component must remain in place during inspection. It is therefore critical to consider additional NDE inspection methods.

Conventional NDE methods include surface examinations using visual testing or penetrant testing, near-surface methods using eddy current testing or magnetic particle testing, and volumetric methods using radiography or ultrasonic testing (UT). Volumetric testing typically provides the most information, so UT is widely used in NDE when it is feasible to do so.

UT techniques provide rapid volumetric examinations that can confirm the material properties (e.g., microstructure size and orientation, elastic moduli, anisotropy, etc.) and component integrity (e.g., geometric conformity and internal defect detection). Importantly, UT methods can be scaled up to address component size and thickness dimensions that are difficult to inspect using XCT or nCT methods. In addition, ultrasonic-based methods are routinely deployed for in-service inspections to understand the impact of service life conditions on component or material integrity. UT is ubiquitous, well-understood, inexpensive, and readily deployable. The main drawbacks of UT are that it has lower spatial resolution than CT methods for detection of fine defects or porosities and that coarse-grained material microstructures can inhibit propagation of ultrasonic energy.

As summarized in the FY23 AMMT NDE report, there are several challenges unique to materials and components fabricated from AM processes that influence the ability to perform NDE (Montgomery et. al., 2023b). These include:

- Surface roughness
- Anisotropic microstructure and mechanical behavior
- Geometric complexities
- Inspection regions (weld vs. entire part, volumetric vs. surface, etc.)
- Unique imperfections/defect structures
- Critical flaw size
- Lack of experience with new in-service defect formation and degradation modes.

The development of NDE capabilities for AM parts will need to address these challenges as an important step in using these capabilities to demonstrate components meet the requirements of safety critical applications. Combined with tackling these technical challenges, other areas that will need consideration include the development of qualification and quantification processes to demonstrate techniques can meet detection resolution and training to qualify instrument operators.

Components produced using materials from AM methods that will be part of advance reactor systems will be subject to the requirements of periodic inspection and testing as safety critical components (classified as Structures, Systems, and Components, SSCs by the NRC). American Society of Mechanical Engineers (ASME) Section XI Division 2 – Requirements for Reliability and Integrity Management (RIM) Programs for Nuclear Power Plants describes a process for developing a reliability and integrity management program consistent with traditional pre-service and in-service inspections used in current light-water reactor plants for all types of nuclear power plant systems (ASME 2023). Central to an ASME XI Division 2 RIM program is the Degradation Mechanism Assessment (DMA) and the establishment of a Monitoring and NDE (MANDE) program. The purpose of the DMA is to identify the potential degradation mechanisms for SCCs that are maintained within the RIM program. The MANDE is chosen for the purpose of being able to detect credible degradation mechanisms expected within materials and components as part of their service life. A MANDE approach must be developed and

demonstrated prior to implementation within a reactor system RIM program to establish the confidence level for detecting damage mechanisms.

The approach to support the use of ASME XI Division 2 RIM program as part of the AMMT post-process NDE activities is outlined in Figure 2. The efforts are primarily focused on establishing the capabilities to characterize material microstructure, mechanical properties, and the presence of defects and porosity. The challenges introduced from advanced manufacturing methods such as LPBF and DED are being assessed and NDE techniques are being explored that will inform the development of MANDE programs for advanced reactors.

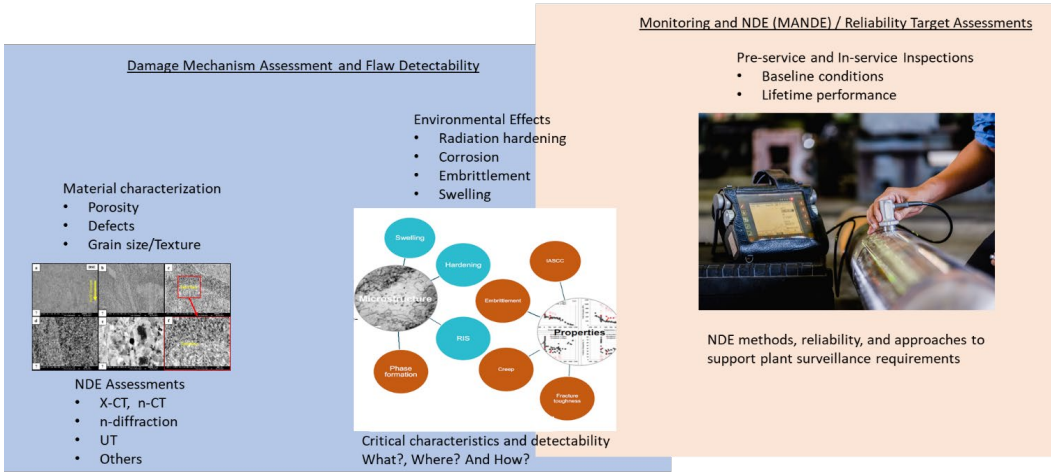

Figure 2. NDE R&D to support RIM for AM Methods and Materials in advanced reactors.

1.3 Summary of FY24 Post-Process NDE Activities

The post-process NDE activities in the AMMT consists of a multi-laboratory collaboration that includes both LPBF and DED AM fabrication processes and a suite of NDE modalities to characterize the final condition of the material and components. Figure 3 provides a schematic of this multi-organizational collaborative effort to perform post-process NDE of AM materials and understand the impact to support component future reliability assessments. As can be seen, the work supporting the post-process NDE spans at least seven different AMMT work packages. Also shown in the figure is the NDE of AM Technical Exchange hosted by the Nuclear Regulatory Commission (NRC) in 2023 and the Electric Power Research Institute in 2024. These workshops are attended by representatives from industry, regulatory, and DOE national laboratories. At the second workshop, the technical exchange discussed the challenges associated with NDE of components fabricated with AM processes, including the lack of specification of applicable codes and standards, limitations of established NDE techniques to address uniqueness of AM component characteristics (e.g. microstructure), and detection of the range of defect types and their evolution during operational performance. The need for further research and development on both the post-process and in-service inspection of AM components was acknowledged by the working group.

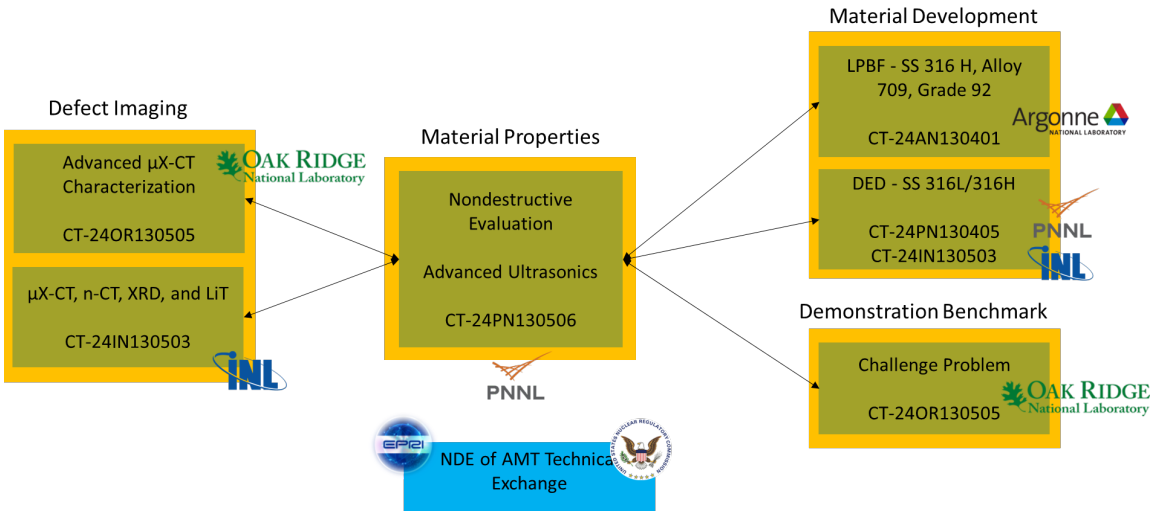

Figure 3. Diagram Highlighting the Multi-Lab Collaboration in AMMT to Perform Post-Process NDE of AM Materials and Understand the Impact for Component Reliability Assessments

The overarching objective of the post-process NDE activities in the AMMT Program is to develop advanced, reliable, and high resolution techniques for evaluation of components fabricated from AM process for use in applications that include safety critical components. During the last two years this collaboration has been focused on assessing different modalities of NDE to characterize the material characteristics of coupons and components fabricated using AM processes (Montgomery et. al., 2023a, Chuirazzi et. al., 2023). These activities span the range of examination techniques from the angstrom scale to the engineering scale. A variety of materials ranging from stainless steel (SS) 316L and 316H to ferritic/martensitic Grade 92 steel produced using LPBF or DED have been evaluated using several modalities of NDE to provide information on microstructure, mechanical properties, porosity and/or defect distributions and geometric conformity.

The laboratory-based methods of NDE have the intention of working at the lower length scale regimes to provide information on microstructure and defect morphologies. The lab-scale techniques included X-ray CT and diffraction, neutron CT and diffraction, lock-in thermography (LIT), and positron annihilation spectroscopy (PAS). The use of these methods can provide information on the material characteristics ranging for atomic lattice vacancy distributions to shape, size, and distributions of defects within material coupons generated from AM process.

The activities at the engineering scale have the goal of utilizing UT methods to yield information on the material properties and the presence of defects within AM fabricated materials and components. A key benefit of applying ultrasonic based techniques is to provide rapid volumetric examinations that can confirm the material properties and component integrity (i.e. porosity and defect detection). UT-based approaches are scalable techniques to address component size and thickness dimensions that are difficult to inspect using higher resolution XCT or other lower length scale visualization methods. This scalable approach builds on developing correlations between lower length scale and engineering scale detection capabilities.

The remainder of this report provides a summary of the R&D activities performed to apply advanced NDE methods to AM materials and components.

2.0 PNNL Ultrasound-based Methods

UT is a well-established and widely used NDE method that is applied in the nuclear industry for both pre-service and in-service examinations of reactor piping and components manufactured using conventional methods (Jacob et.al. 2020). This is a volumetric method to detect and measure cracks, flaws, voids, corrosion, density, porosity, and grain structures in regions of concern, e.g., weld and heat affected zones. UT methods use a variety of techniques to apply and monitor high frequency sound waves that detect the reflections or perturbations of these sound waves from defects, flaws, or other microstructural discontinuities. As part of the AMMT program, PNNL has applied pulse-echo measurements, RUS, acoustic microscopy, and reflected amplitude spectrum analysis to evaluate elastic mechanical properties, microstructure variations, and geometric conditions.

The following summarizes the results of the FY24 activities performed to evaluate the material characteristics of material and components fabricated using both LPBF and DED additive manufacturing methods. First, several material coupons produced using LPBF and DED techniques were examined using pulse echo methods and resonant ultrasound spectroscopy to obtain information on the mechanical properties for comparison to available literature information. Second, a technique using an analysis of reflected ultrasonic waves was applied to generate a detailed contour map of the wall thickness of a DED 316L cylindrical component with different levels of surface condition.

2.1 Material Property Assessments

Ultrasonic examinations were performed on a series of coupons fabricated using LPBF or DED AM methods to evaluate the material condition and elastic mechanical properties. The information gained from these examinations will assist in assessing the challenges that will need to be considered for conducting NDE on full-scale components prepared with these techniques.

Table 2 provides a list of the material coupons received from ANL and INL that were examined using UT methods. The material types included SS grade 316L (SS316L), Alloy 709 austenitic SS, and Grade 92 ferritic/martensitic SS. The coupons varied in size, and further sectioning and surface preparation were applied to facilitate the UT exams in some cases.

Table 2. Additive Manufactured Coupons Examined Using Ultrasonic Testing

Material Type	Fabrication Method	Nominal Coupon Size	Number of Coupons
A709	ANL-LPBF	30 mm x 38 mm x 10 mm wall thickness 3 – 3.5 mm	1
Grade 92	ANL-LPBF	10 mm x 10 mm x 3-5 mm	9
SS316L	INL-DED	9 mm x 5.7 mm x 5 mm	2

The elastic mechanical properties of the material coupons were obtained by measuring the longitudinal and shear velocities using ultrasonic methods. Due to the size of the coupons, the elastic mechanical properties were obtained in a single direction/dimension that afforded the ability to measure the ultrasonic velocities. The surface area of the coupon limited the examinations to the sides large enough to accommodate the ultrasonic probes. Generally, the longitudinal velocities were measured perpendicular to the build direction. Two shear velocities (parallel and perpendicular to the build direction) were measured as shown in Figure 4.

Ultrasonic velocity measurements were obtained using a longitudinal (compression) wave probe and a normal incidence shear (transverse) wave probe that was used at 0 and 90 degree orientations. Pulse-echo mode was used to determine the time-of-flight (ToF), which was combined with the dimensional measurement of the sample thickness to calculate the longitudinal (V_l), and shear (V_{S1} and V_{S2}) velocities.

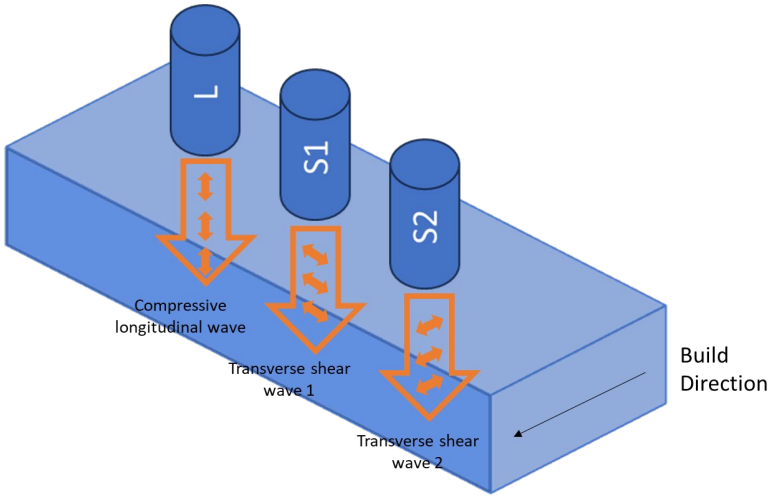

Figure 4. Schematic of longitudinal and shear time-of-flight and velocity measurement approach in relationship to the build direction for the coupons.

Once the ultrasonic velocities were obtained for the different material coupons or specimens, the elastic mechanical properties were computed using relationships for isotropic material behavior (Krautkrämer 1990). For an isotropic material, the Poisson's ratio (υ) can be estimated from the longitudinal (V_l) and shear velocities (V_S) by:

$$\upsilon = \frac{1 - 2\left(\frac{V_s}{V_l}\right)^2}{2 - 2\left(\frac{V_s}{V_l}\right)^2} \quad (1)$$

The shear modulus (G) is calculated from the shear velocity (V_S) and material density (ρ) using;

$$G = \rho V_s^2 \quad (2)$$

The elastic (Young's) modulus (E) is calculated using the longitudinal velocity (V_l), the material density (ρ) and Poisson's ratio (υ) using the following relationship.

$$E = \frac{V_l^2 \rho (1 + \upsilon)(1 - 2\upsilon)}{(1 - \upsilon)} \quad (3)$$

Lastly, the bulk modulus is calculated using the longitudinal and shear velocities and the material density with the following relationship:

$$B = \rho\, V_l^2 - \frac{4}{3}(\rho V_s^2) \tag{4}$$

In the situation where the two measured shear velocities were different due to anisotropic behavior, two sets of elastic mechanical properties were approximated to yield some insights into the directionally dependent material behavior.

2.1.1 LPBF Alloy 709 Specimen

A remnant of Alloy 709 from a LPBF build was received from ANL for examination using ultrasonic methods. A description of the LPBF system and build parameters can be found in Zhang 2023. The remnant came from Sample 3 listed in the reference and had been machined using EDM by ANL to extract miniature tensile specimens. Figure 5 contains two pictures of the as-received coupon (a) a side view along the build direction and (b) a top view showing the region where tensile specimens were removed. The coupon dimensions were 30 mm wide, 38 mm tall, and 10 mm deep.

(a) 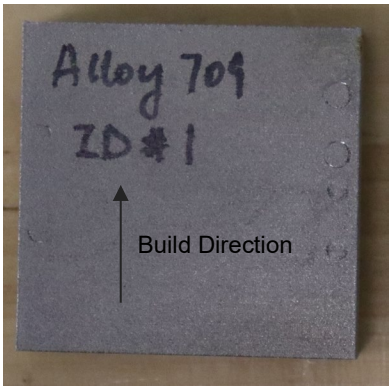

(b) 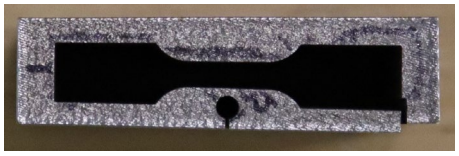

Figure 5. LPBF Alloy 709 as-received coupon. (a) long side with build direction indicated and (b) top view showing area with tensile specimens removed.

The left and right ends of the coupon (seen in Figure 5b) were removed resulting in two specimens (Specimen 1 and Specimen 3) with approximate dimensions of 10 mm wide by 38 mm long by 3 mm thick. The larger pieces (Specimen 2 and Specimen 4) were set aside for examination at a later time with alternative ultrasonic methods. Photographs of Specimen 1 and 3 are shown in Figure 6. Each specimen had three locations designated along the build direction as marked in Figure 6. UT examinations were performed at each of the three locations.

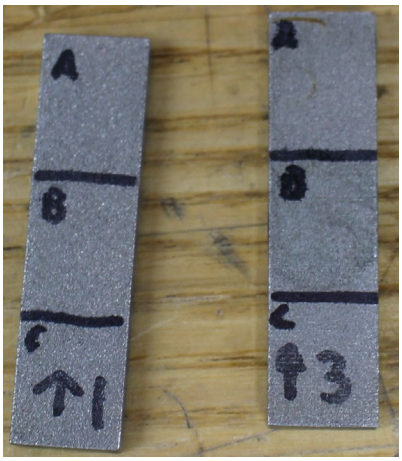

Figure 6. LPBF Alloy 709 Specimens 1 and 3 removed from coupon for ultrasonic testing. The examination locations along the build direction are indicated.

Dimensional measurements were performed at the three locations for both Specimen 1 and 3 from the A709 coupon. The Archimedes method was used to obtain the density for each specimen, and the density was assumed to be constant throughout the specimen for estimates of the elastic mechanical property calculations for the three locations.

Pulse-echo ultrasonic measurements at 5 MHz were used to determine the longitudinal and shear velocities at each location (A, B, and C) of the two specimens. To account for measurement variability, five (5) measurements were made at each location for the ToF and specimen thickness. From these measurements, the longitudinal and shear velocities were calculated as two times the thickness divided by the ToF. The average measurements are shown in Table 3. Estimates of the uncertainties in the ultrasonic velocities and the standard deviation in the material density measurements are included in Table 3 for reference. Similar uncertainties in the ultrasonic velocity values are seen across all values reported herein. The shear velocity values exhibit a consistent and measurable difference of 1% to 2% between the two orthogonal directions, suggesting anisotropic material behavior. Further work is needed to identify the direction of the material anisotropy relative to the build direction.

Table 3. LPBF Build Parameters and Ultrasonic Velocities for the Alloy 709 Specimens

Sample	Power (W)	Exposure (µs)	Hatch Space (µm)	Point Distance (µm)	Layer Thickness (µm)	Energy Density (J/mm^3)	Long. Velocity (m/s)	Shear Vel. 1 (m/s)	Shear Vel. 2 (m/s)	Density (g/cm^3)
1A	195	70	110	60	50	49.63	5792 (30)[1]	3134 (15)	3085 (17)	7.938 (0.010)[2]
1B	|	|	|	|	|	|	5812 (34)	3131 (15)	3087 (18)	7.938 (0.010)
1C	|	|	|	|	|	|	5803 (45)	3138 (26)	3092 (23)	7.938 (0.010)
3A	|	|	|	|	|	|	5817 (61)	3126 (38)	3066 (31)	7.937 (0.003)
3B	|	|	|	|	|	|	5773 (13)	3112 (21)	3031 (8)	7.937 (0.003)
3C	|	|	|	|	|	|	5794 (45)	3119 (23)	3064 (27)	7.937 (0.003)

[1] – Ultrasonic velocity uncertainty calculated from propagation of errors in ToF and dimensional measurements

[2] – Standard deviation in Archimedes density measurements

The ultrasonic velocities shown in Table 3 were used to estimate the elastic mechanical properties using the relationships in Equations 1 through 4. As noted, the relationship between ultrasonic velocity and elastic mechanical properties assumes isotropic material behavior. As a result, two sets of mechanical properties were computed for each shear velocity value. Table 4 summarizes the Poisson's Ratio and Shear Modulus calculated for each of the shear velocities. A difference of about 3% is seen between the two datasets. Table 4 contains the Young's Modulus and Bulk Modulus calculated for the Alloy 709 material. Similar differences are noted for these values computed from the two shear velocity measurements.

Table 4. Poisson's Ratio and Shear Modulus Calculated from the Measured Ultrasonic Velocities for the Alloy 709 Specimens

Sample	Poisson's Ratio 1 (--)	Poisson's Ratio 2 (--)	Shear Modulus 1 (Gpa)	Shear Modulus 2 (Gpa)
1A	0.293	0.302	77.9	75.5
1B	0.296	0.304	77.8	75.6
1C	0.293	0.302	78.2	75.9
3A	0.297	0.308	77.6	74.6
3B	0.295	0.310	76.8	72.9
3C	0.296	0.306	77.2	74.5

Table 5. Young's Modulus and Bulk Modulus Calculated from the Measured Ultrasonic Velocities for the Alloy 709 Specimens

Sample	Young's Modulus 1 (Gpa)	Young's Modulus 2 (Gpa)	Bulk Modulus 1 (Gpa)	Bulk Modulus 2 (Gpa)
1A	202	197	162	166
1B	202	197	164	167
1C	202	198	163	166
3A	201	195	165	169
3B	199	191	162	167
3C	200	195	164	167

The Young's Modulus, Poisson's Ratio, and Bulk Modulus obtained from the ultrasonic examinations for the LPBF Alloy 709 specimens are compared to literature values contained in Reese 2021 for wrought material in a set of box and whisker plots. The box and whisker plots provide information on the statistical nature of the data presented, including the 1st (25%) and 3rd (75%) quantile range, the median, and the minimum/maximum interquartile range. Outliners are highlighted when present in the dataset. The plots show a limited estimation of the differences in the properties between the material produced using AM methods from the traditionally manufactured material. It is recognized that the amount of information obtained through this work is limited and further data is needed to improve the statistical comparison.

Figure 7 contains a comparison of the Young's Modulus measured in this work with those for wrought material. The LPBF Alloy 709 has a higher Young's Modulus value based on the Shear 1 velocity measurements as compared to the wrought material. It is also seen that the LPBF Alloy 709 material exhibits move variability in the elastic properties. Similar observations are seen in Figure 8 and Figure 9 for the Poisson's Ratio and the Bulk Modulus comparisons to wrought material. The comparison to literature values for Alloy 709 indicate that the LPBF material has a measurably higher stiffness than wrought fabricated material. Further work is required to identify the causes of the material differences.

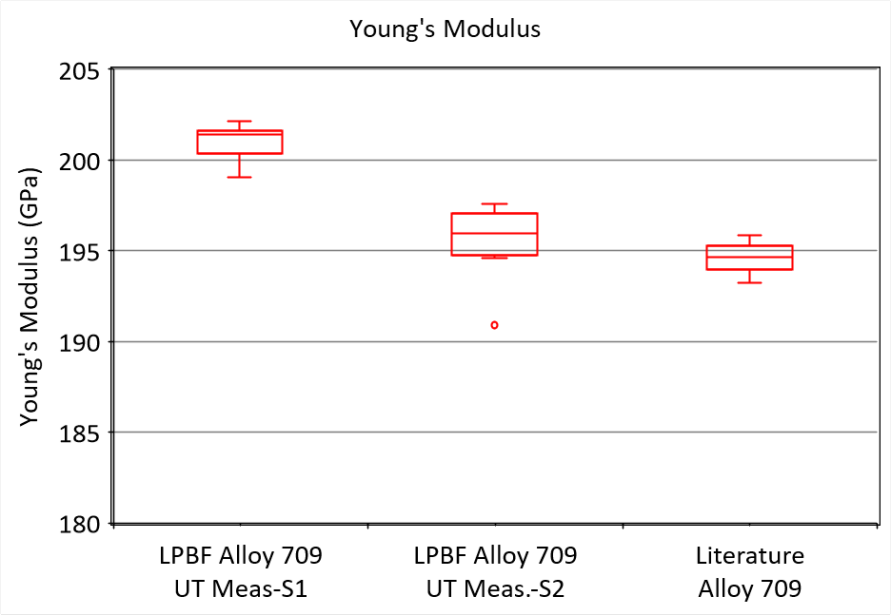

Figure 7. Comparison of Young's Modulus for LPBF Alloy 709 and wrought Alloy 709 from the literature.

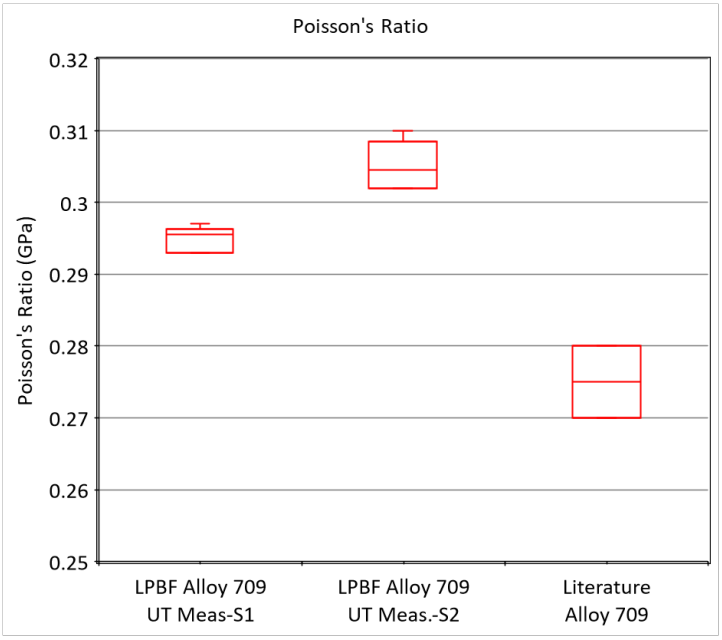

Figure 8. Comparison of Poisson's Ratio for LPBF Alloy 709 and wrought Alloy 709 from the literature.

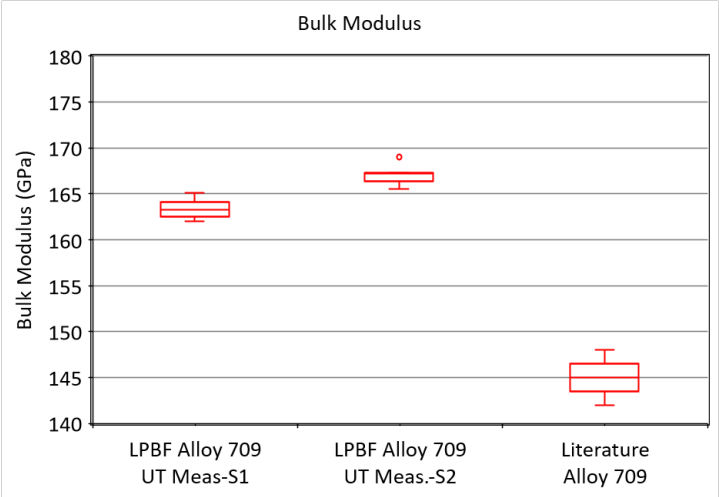

Figure 9. Comparison of the Bulk Modulus for LPBF Alloy 709 and wrought Alloy 709 from the literature.

2.1.2 LPBF Grade 92 Coupons

Nine (9) coupon specimens of LPBF Grade 92 (Gr92) for examination using ultrasonic techniques were received from ANL (Zhang 2023). Gr92 is a ferritic/martensitic steel alloy material with 9% chromium, 2% tungsten, and 0.5% molybdenum alloy elements to improve high temperature creep behavior (Zhang 2023). The as-fabricated specimens are nominally 10 mm high x 10 mm wide with thicknesses varying between 3 mm and 5 mm. Figure 10 provides a photograph of the 9 specimens showing the geometric conditions. Specimen #1 had been sectioned by ANL prior to shipment to PNNL resulting in the polished aspect shown in the figure. The build direction was assumed to progress in the direction away from the sawtooth features at the bottom of each specimen.

Each of the specimens were fabricated with different process parameters used in the LPBF system. Table 6 lists the process parameters for each coupon as provided in Zhang 2023. Specimen coupon #3 was used for destructive examinations at ANL and is not included in the ultrasonic examinations. The process parameters for coupon #3 are included for completeness in the analysis presented herein.

Results for the ultrasonic velocity measurements for the LPBF Gr92 specimens are listed in Table 7 along with the coupon material density obtained using the Archimedes method. The ultrasonic velocity and density results presented in Table 7 are the average from six trials for longitudinal and shear velocities and ten measurements for material density. Standard deviations in the measurements for longitudinal velocity and density were well below 1%. The standard deviation in the shear velocities was above 2% due to larger variability in this measurement.

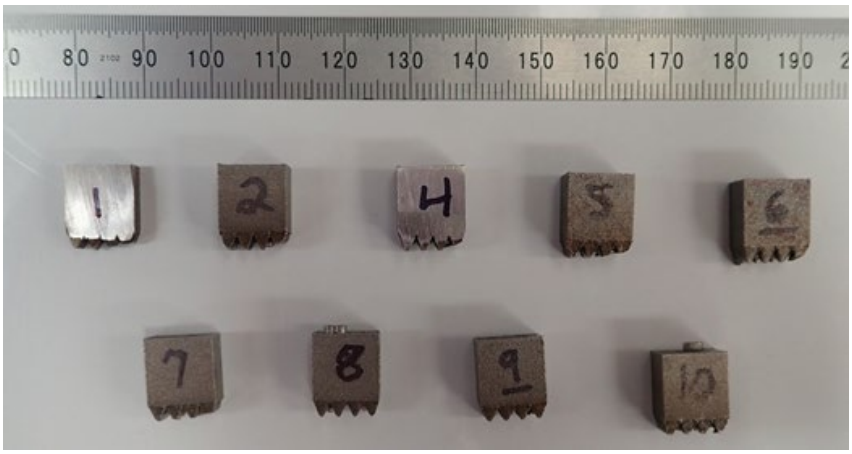

Figure 10. LPBF Grade 92 Specimens Examined Using Pulse Echo Ultrasonic Methods

Table 6. LPBF Process Parameters for the Grade 92 Coupons Examined Using Ultrasonic Methods

Sample	Power (W)	Exposure (µs)	Hatch Space (µm)	Point Distance (µm)	Layer Thickness (µm)	Energy Density (J/mm^3)
1	221	101	110	55	50	73.8
2	185	101	110	45	50	75.5
3[1]	*270*	*80*	*110*	*50*	*50*	*78.5*
4	200	100	110	45	50	80.8
5	305	75	110	50	50	83.2
6	165	105	110	55	50	57.3
7	220	62	110	45	50	55.1
8	180	110	110	60	50	60.0
9	200	95	110	55	50	62.8
10	225	95	110	60	50	64.8

[1]- ANL performed destructive exams on Specimen 3. The build parameters included for completeness.

The published density for Gr92 fabricated using traditional fabrication methods is 7.871 g/cm^3 (Hasegawa 2014). The density measurements for the LPBF Gr92 specimens indicate that some level of porosity may be present in the specimens, ranging between 0.7% and 2%.

The shear velocities presented in Table 7 are 90º orthogonal to each other and perpendicular to the build direction as shown in Figure 4. Material anisotropy is seen in the shear velocity measurements with the largest differences noted in Specimens 1, 5, and 10. The variation between the two shear velocities range between 2% and 4%. The remainder of the specimens exhibited differences between the two shear velocities that are below 0.5%, suggesting a more isotropic material microstructure.

Table 7. Ultrasonic Velocity Measurement Results for the Grade 92 Coupons

Sample	Long. Velocity (m/s)	Shear Velocity 1 (m/s)	Shear Velocity 2 (m/s)	Density (g/cm^3)
1	6251 (55)	3405 (120)[1]	3348 (55)	7.807 (0.010)[2]
2	6013 (17)	3282 (5)	3288 (5)	7.789 (0.009)
3	--	--	--	--
4	6137 (89)	3340 (31)	3347 (30)	7.722 (0.012)
5	5983 (33)	3385 (6)	3253 (0)	7.805 (0.012)
6	6011 (9)	3297 (8)	3301 (5)	7.801 (0.010)
7	6016 (18)	3301 (7)	3297 (4)	7.817 (0.011)
8	6137 (34)	3336 (16)	3350 (16)	7.803 (0.006)
9	6019 (19)	3299 (19)	3256 (7)	7.816 (0.007)
10	5984 (22)	3362 (7)	3272 (6)	7.765 (0.004)

[1]- Ultrasonic velocity uncertainty calculated from propagation of errors in ToF and dimensional measurements.

[2]- Standard deviation in Archimedes density measurements.

The ultrasonic velocities shown in Table 7 were used to estimate the elastic properties from the relationships described in Equations 1 through 4. As noted, the relationship between ultrasonic velocity and elastic mechanical properties assumes isotropic material behavior. As a result, two sets of mechanical properties were computed for each shear velocity direction measurement. Table 8 provides the calculated Young's Modulus and Poisson's Ratio for the Gr92 coupons from the ultrasonic velocity and density measurements. Variations in the elastic mechanical properties for the coupons are noted between the different process parameters used in the LPBF process.

Table 8. Young's Modulus and Poisson's Ratio Calculated for the Grade 92 Coupons

Sample	Young's Modulus 1 (GPa)	Young's Modulus 2 (GPa)	Poisson's Ratio 1 (--)	Poisson's Ratio 2 (--)
1	233	227	0.289	0.299
2	216	214	0.288	0.287
3	--	--	--	--
4	222	223	0.290	0.288
5	226	213	0.265	0.290
6	218	218	0.285	0.284
7	219	218	0.285	0.285
8	224	226	0.290	0.288
9	219	217	0.285	0.287
10	223	214	0.269	0.287

A comparison of the Young's Modulus obtained from the ultrasonic measurements and the laser power used to fabricate the coupons is shown in Figure 11. The comparison in Figure 11 indicate only a weak dependence of the elastic mechanical properties on the laser power used in the LPBF process. The effect of the anisotropic shear velocities on the Young's Modulus can be seen in this figure for coupons #1, #5, and #10. These three coupons were fabricated at the highest laser powers, suggesting that microstructural features created during the melting and cooling process may be influencing the shear velocities. To further understand the anisotropic behavior in the elastic properties of the Gr92 coupons, the difference in the Young's Modulus was used to calculate an Anisotropy Factor. The factor ranges from 5.75% for Coupon #5 down to 0.2% for Coupon #6. A comparison of this factor with the LPBF energy density used to fabricate the coupons is shown in Figure 12. A trend in the amount of process-induced anisotropic behavior with energy density may be seen in this figure; however, further work is needed to better understand the impact of the LPBF process parameters on the anisotropic mechanical behavior the Gr92 material.

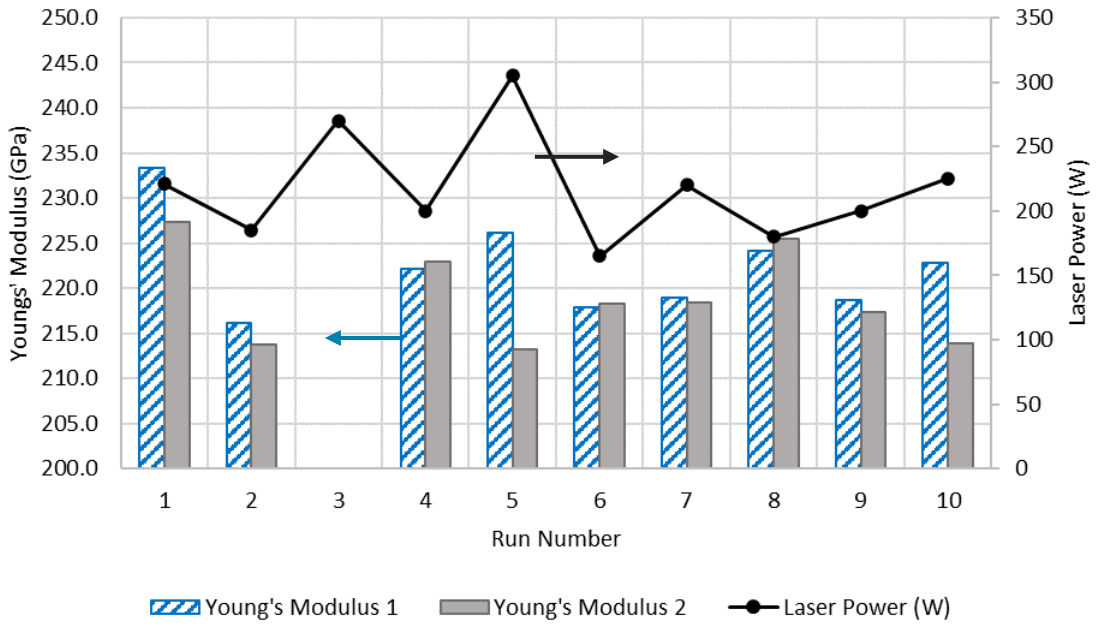

Figure 11. Young's Modulus for Grade 92 Coupons Compared to the Laser Power Used in the LPBF Fabrication Process of Each Coupon. Arrows indicate relevant ordinate axis for the data.

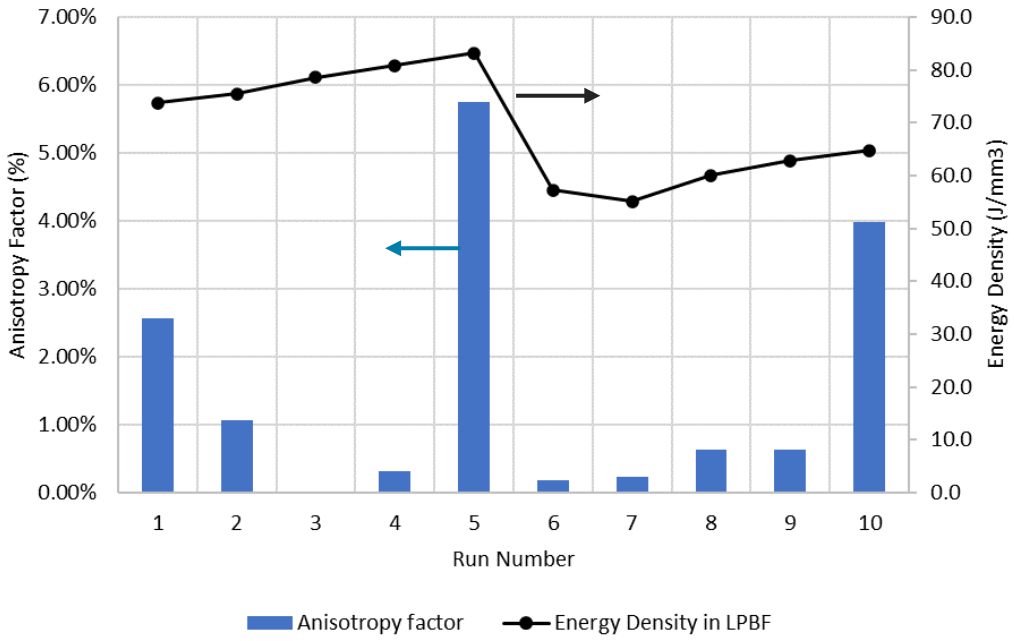

Figure 12. Anisotropy Factor for the Grade 92 Coupons Compared to the Energy Density Used in the LPBF Process. Arrows indicate relevant ordinate axis for the data.

The Young's Modulus and Poisson's ratio for Grade 92 material from standard fabrication and thermal treatment are available in Hasegawa 2014. A comparison of the elastic mechanical properties from the LPBF Gr92 and the available literature information (a single value) at room temperature are shown in Figure 13 and Figure 14. Compared to standard material, a few of the samples of the LPBF Gr92 material have a higher Young's Modulus and lower Poisson's Ratio than the values reported in the literature. Some process parameters produce material with

similar mechanical properties between the LPBF and traditionally fabricated material. These results may indicate that the microstructure arising from the LPBF process influences the solid solution strengthening of the LPBF Gr92 coupons as compared to the standard material. Further work is needed to correlate the resulting microstructure from the LPBF fabrication process with the measured elastic properties.

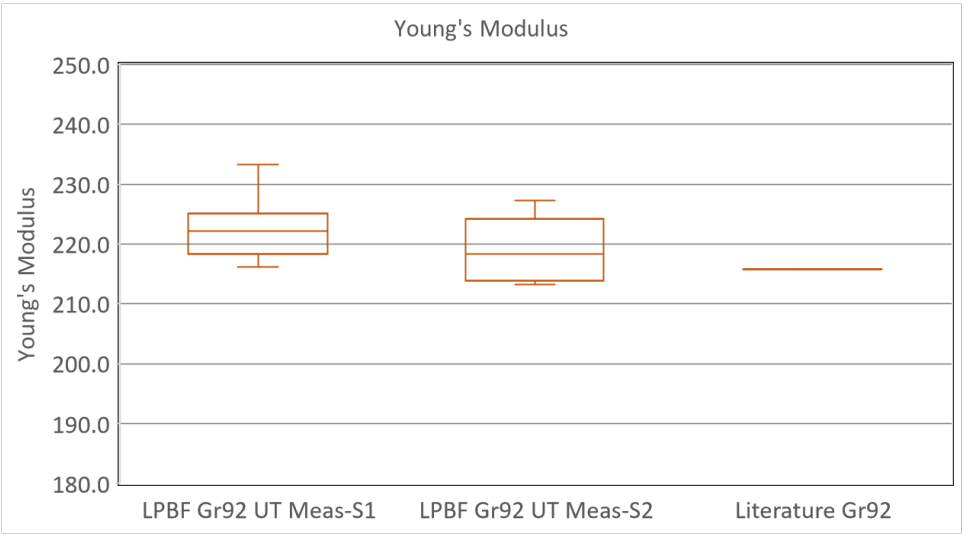

Figure 13. Comparison of Young's Modulus for the LPBF Grade 92 Coupons with Literature Data Reported in Hasegawa 2014

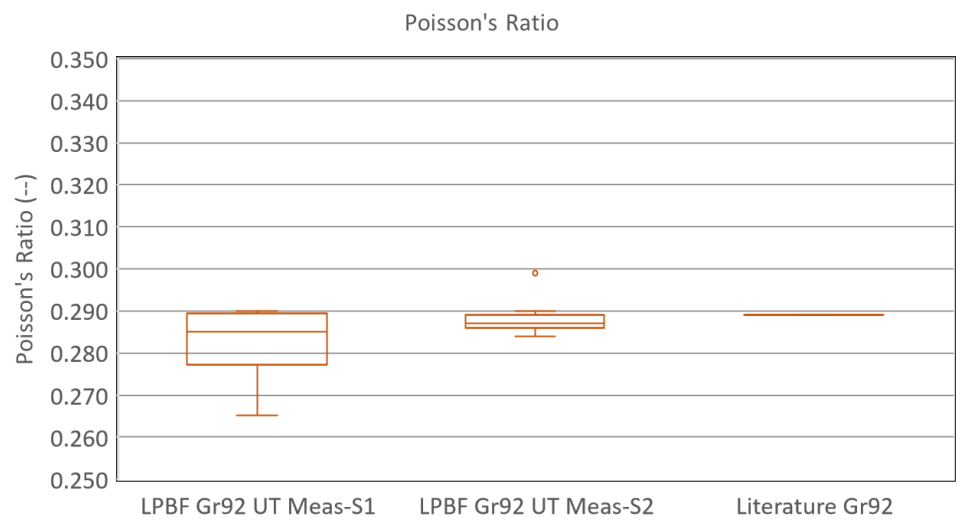

Figure 14. Comparison of Poisson's Ratio for the LPBF Grade 92 Coupons with Literature Data Reported in Hasegawa 2014

2.1.3 DED 316L Coupons

Two SS316L coupons fabricated using powder laser DED were received from INL for examination with advanced UT methods. A series of powder laser DED coupons was prepared using a variety of process parameters that yielded fabrication defects and different levels of porosity. Previously, these coupons were examined using XCT methods, and the results from

these examinations are summarized in Chuirazzi et. al., 2023. Table 9 presents the key features of the two DED 316L coupons examined using UT methods. The build direction was assumed to be along the L-axis (long axis). The coupon thickness (T) was assumed to be the smallest dimension of the cuboids for consistent reference.

Table 9. Characteristics of the Powder Laser DED 316L Coupons

Coupon ID	Dimensions L x W x T (mm)	Porosity from X-ray CT (%)	Archimedes Coupon Density (g/cm^3)	RUS Coupon Density (g/cm^3)
INL-DED-1	9.41 x 5.56 x 5.26	1.64	7.86 (0.03)[1]	7.886
INL-DED-2	9.12 x 5.71 x 5.68	3.83	7.80 (0.02)	7.653

[1] – Standard deviation in Archimedes density measurements

The bottom surfaces of the as-received coupons had features that made conducting the UT examinations difficult. To facilitate the UT examinations of these two coupons, surface machining was performed on the bottom end of the samples to remove some of the surface roughness. Figure 15 and Figure 16 contain optical images of the machined bottom ends highlighting the final surface conditions and examples of the surface breaking porosity features present in the coupons.

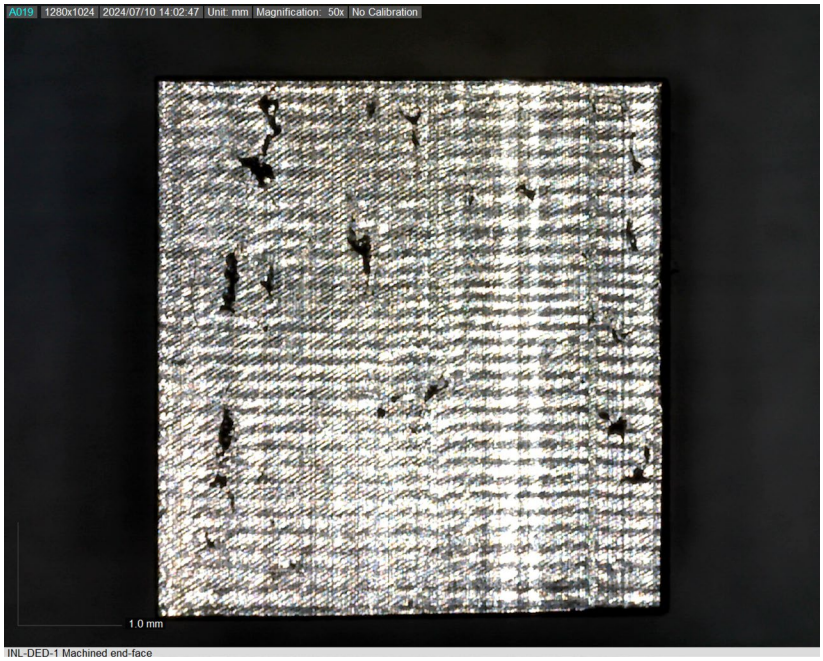

Figure 15. Machined End of INL-DED-1 Coupon with Surface Breaking Porosity/Defects

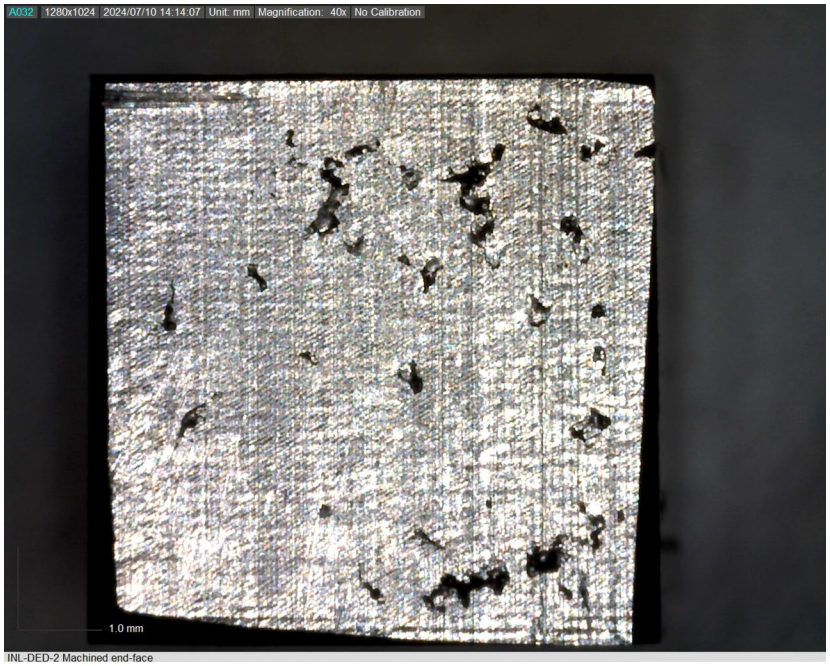

Figure 16. Machined End of INL-DED-2 Coupon with Surface Breaking Porosity/Defects

A comparison of the coupon side view optical images is show in Figure 17 for a) INL-DED-1 and b) INL-DED-2. Two long open pores/defects are seen in Figure 17b near the lower end of INL-DED-2. These features are consistent with the location of porosity/defects seen in XCT imaging of this coupon. Based on the XCT imaging in Chuirazzi et. al., 2023, the porosity appears to be more prevalent near the region adjacent to the build plate and reduces as the distance along the build direction increases. Similar surface breaking defects are seen on the remaining side optical images for INL-DED-1 and INL-DED-2.

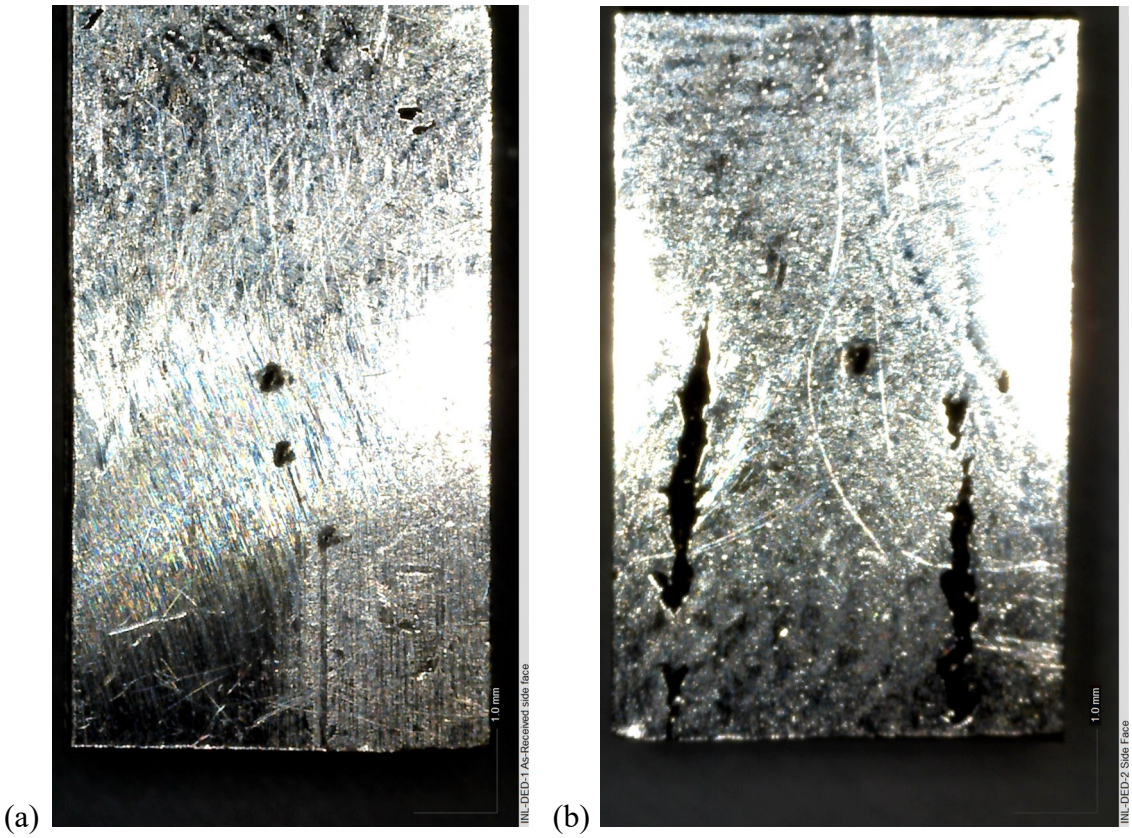

Figure 17. Side View of DED 316L Coupons with Surface Breaking Porosity: (a) INL-DED-1 Coupon and (b) INL-DED-2 Coupon

The DED 316L coupons were examined using pulse-echo ultrasonic velocity measurements, acoustic microscope imaging, and RUS. The influence of the porosity/defects within the coupons was noted in each of the UT techniques. The following summarizes the preliminary observations from these examinations.

Results for the longitudinal and shear velocities obtained from the pulse echo ToF measurements are summarized in Table 10 for the two DED 316L coupons. The size of the coupons allowed for ToF measurements to be made on all three directions (Length (L), Width (W), and Thickness (T)). The measurement of the shear velocities was influenced by the presence of the porosity/defects present in the coupons. A single shear velocity measurement in the length direction was obtained for the INL-DED-1 coupon, and no shear velocity measurements were successful for the INL-DED-2 coupon.

Using the ultrasonic velocity values shown in Table 10 for the INL-DED-1 coupon, the elastic mechanical properties were computed from Equations 1 through 4. The values shown in Table 11 were determined by averaging the results calculated for the two different shear velocities. The UT examinations demonstrate that the presence of porosity/defects in the material is impacting the elastic mechanical properties in the coupon. The biggest effect is seen in the measurements made in the build direction (INL-DED-1-L). As was found in the XCT imaging performed at INL and in the acoustic microscope results presented below, the localization of the porosity in the lower region of the coupon adjacent to the build plate has the largest effect on the mechanical properties parallel to the build direction.

Table 10. Results of Pulse Echo Time-of-Flight Measurements for the DED 316L Coupons

Sample	Long. Velocity (m/s)	Shear Velocity 1 (m/s)	Shear Velocity 2 (m/s)	Archimedes Density (g/cm^3)
INL-DED-1-T	5784 (8)	3112 (3)	3058 (2)	7.86 (0.03)
INL-DED-1-W	5789 (14)	2890 (7)	3087 (4)	7.86 (0.03)
INL-DED-1-L	4651 (7)	2892[1]	N/A	7.86 (0.03)
INL-DED-2-T	5096 (16)	N/A[2]	N/A[2]	7.80 (0.02)
INL-DED-2-W	5492 (22)	N/A	N/A	7.80 (0.02)
INL-DED-2-L	4858	N/A	N/A	7.80 (0.02)

1 - Based on single time of flight measurement. Follow on attempts were unsuccessful in measuring the shear velocity in INL-DED-1
2 - Attempts were unsuccessful in measuring the shear velocity in INL-DED-2

Table 11. Elastic Mechanical Properties for INL-DED-1 Calculated from the Ultrasonic Velocity Measurements

Sample	Young's Modulus (GPa)	Shear Modulus (GPa)	Bulk Modulus (GPa)	Poisson's Ratio (--)
INL-DED-1-T	194.7	74.81	163.3	0.301
INL-DED-1-W	185.1	70.31	169.7	0.318
INL-DED-1-L	155.8	65.76	82.4	0.185

The DED 316L coupons were scanned in an acoustic microscope to assess the internal defect structure within the material. The pulse echo scans were performed with the OKOS VUE-400-P Acoustic Microscope using a 20 MHz probe combined with a 50 micron x 50 micron scanning resolution. Acoustic C-scan results were post-processed to obtain contour maps of the acoustic signal reflection amplitudes.

Preliminary results from the acoustic microscope scans are provided in Figure 18 and Figure 19 for INL-DED-1 and INL-DED-2. Two different orientations are shown for the scans performed in the L-W (A1 scan) plane and the L-T (A2 scan) plane. Porosity/defects reduce the amplitude of backwall reflections and produce a darker region in the scan images shown. Some edge effects (such as speckle and diminished signal intensity) are seen in the images related to the method used to perform the scans and the software processing and can be ignored in these preliminary results. For the INL-DED-1 coupon shown in Figure 18, porosity/defects are observed in the bottom region of the coupon that is thought to be adjacent to the build plate. The upper 2/3rd of the coupon appears to be mostly defect-free or contains defects below the scan resolution. These results are consistent with the pulse-echo ToF measurements conducted in the T and W directions, which indicate a limited impact of porosity on the ultrasonic velocities in this region of the coupon.

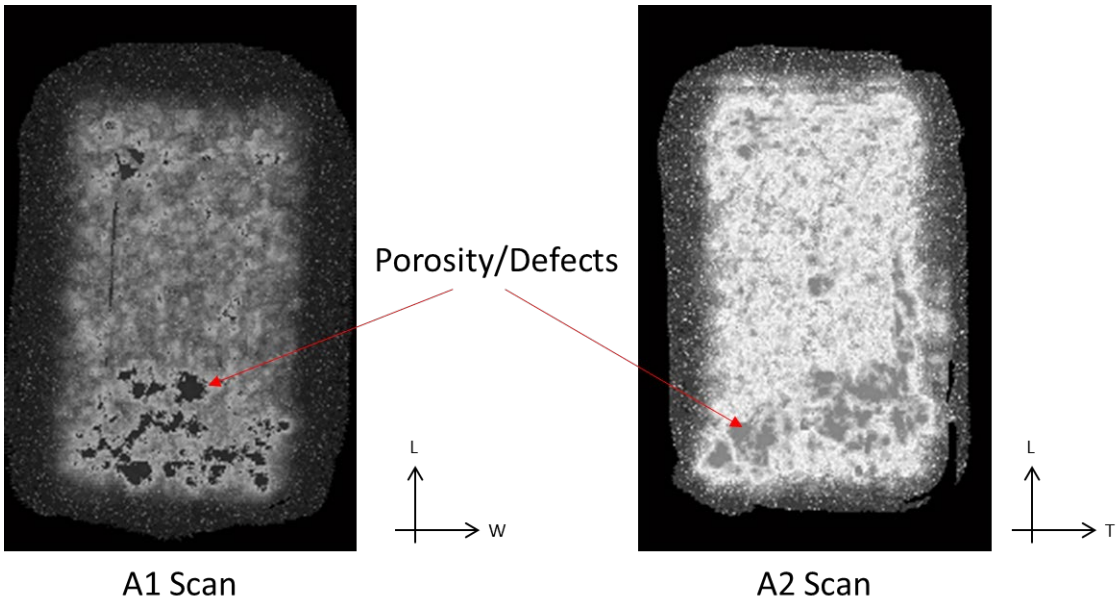

Figure 18. Acoustic Microscope Scan Images Showing the Porosity/Defects in the INL-DED-1 coupon. The Porosity/Defects are dark gray/black in the images.

The acoustic microscope images for INL-DED-2 shown in Figure 19 contain a higher percentage of porosity/defect features in both the A1 and A2 scans. The porosity/defect structure is denser in the lower region of the coupon, similar to INL-DED-1. However, porosity/defects are also observed into the upper regions of the coupon in the INL-DED-2 sample. The extensive distribution of the porosity/defect structures will have a pronounced impact on the apparent longitudinal and shear velocities within the coupon and influence the pulse-echo measurement technique due to sound scattering or noise generation.

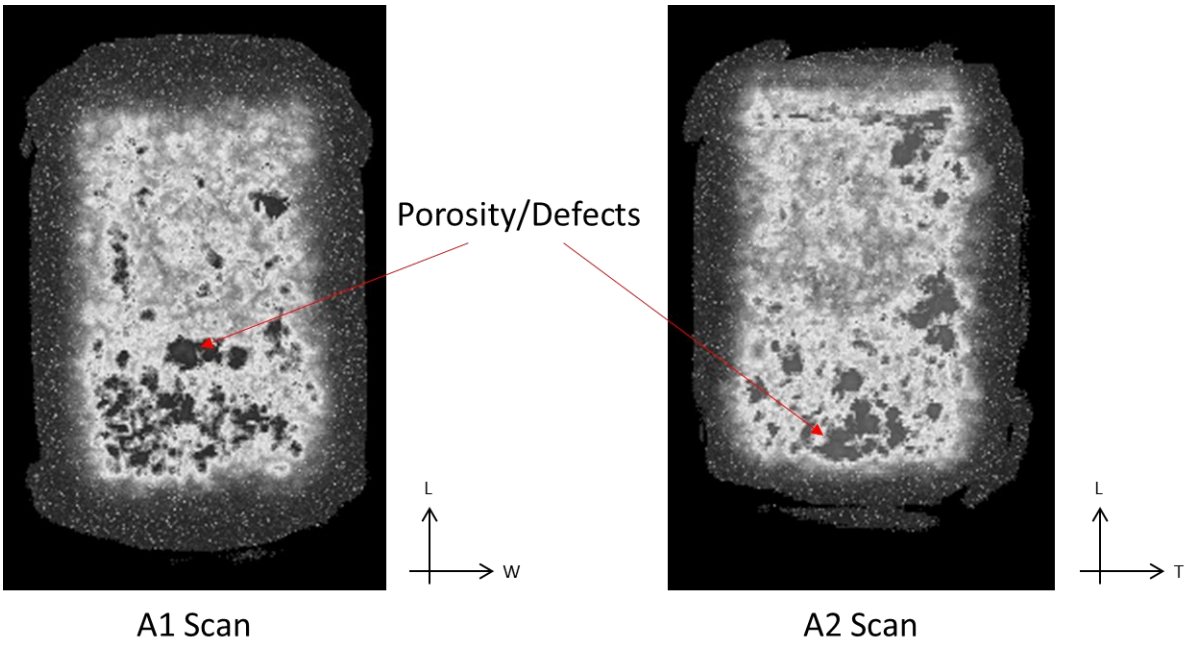

Figure 19. Acoustic Microscope Scan Images Showing the Porosity/Defects in the INL-DED-2 coupon. The Porosity/Defects are dark gray/black in the images.

RUS was performed on the DED 316L coupons to measure the elastic mechanical properties. RUS is a method in which ultrasonic methods are used to excite a coupon of well-defined shape through a range of vibrational frequencies and measure the resonance frequencies. Linear elastic theory relates the resonance frequencies to the material elastic properties, and by using an inverse computational method, the material elastic constants can be obtained from the RUS measurements. Montgomery 2023a provides an overview of the RUS measurement technique and approach to obtain the elastic constants and mechanical properties from the resonance frequencies. A total of fifty (50) resonance frequencies were obtained for each DED 316L coupon. A broad range of frequencies can provide a reduction in the error analysis and ensures that effect of small defects is included in the results.

Figure 20 contains a plot of the resonance frequencies for both the INL-DED-1 and INL-DED-2 coupons across the frequency range of 100 kHz to 500 kHz. The resonance frequencies for INL-DED-2 are shifted relative to INL-DED-1 due to differences in sample geometry, density, and the porosity/defects. Broadening of several frequency peaks is also noted, which is consistent with the presence of defects in the material.

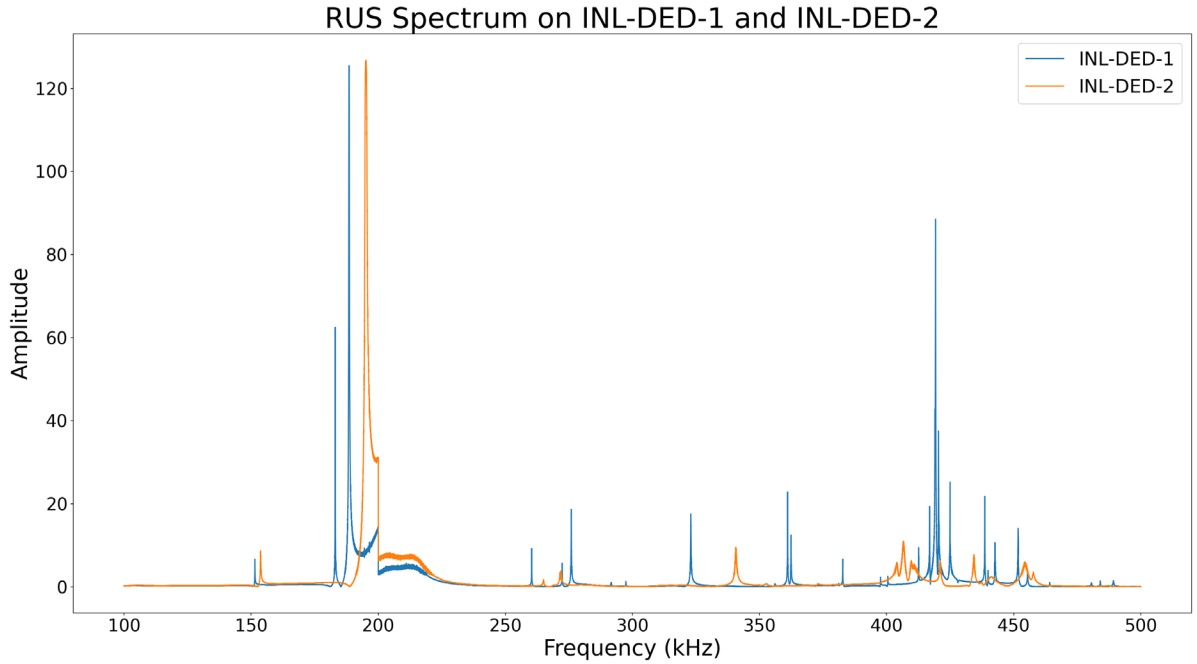

Figure 20. Amplitude versus Frequency from the RUS measurements for the INL-DED-1 and INL-DED-2 Coupons. Resonance Frequencies are Noted by the Peaks

The resonance frequency results shown above are used by the RUS software to estimate the material elastic constants and mechanical properties. The results for the isotropic material model are shown in Table 12 for the DED 316L coupons. Results from RUS measurements on wrought 316L material presented in Montgomery 2023a are also included in Table 12 for comparison. The results indicate that the presence of porosity/defects in the INL-DED-2 coupon appears to affect the elastic constants and mechanical properties. The presence of porosity in the INL-DED-1 coupon has only a small impact on the elastic properties and further evaluations are needed to assess this level of porosity on overall material performance.

Table 12. Elastic Constants from RUS Analysis and Mechanical Properties Computed Using Isotropic Material Relationship

Parameter	INL-DED-1	INL-DED-2	Wrought 316L
C11 (GPa)	242.3	203.7	247.8
C12 (GPa)	90.6	45.9	94.3
C44 (GPa)	74.1	73.2	76.7
Bulk M (K) (GPa)	141.2	98.5	145.5
Shear M (G) (GPa)	74.1	73.2	76.7
Youngs M (E) (GPa)	189.2	176.0	195.7
Poisson Ratio (--)	0.277	0.202	0.276
Density (g/cm^3)	7.886	7.653	8.0[1]

[1] – Nominal material density for SS316L

The RUS measurements provide an estimate of the material density. The values shown in Table 12 differ from the values measured using the Archimedes method and the estimates of porosity from the XCT images. Table 13 provides an estimate of the porosity contained in the DED 316L coupons using three different methods, assuming that the theoretical density of 316L is 8.0 g/mm^3. For coupon INL-DED-1, the results are similar between the three methods suggesting that the amount of surface breaking porosity is small. The situation is different for the INL-DED-2 coupon, which exhibits significant surface breaking porosity. The Archimedes method appears to appreciably underestimate the porosity due to water ingress into the surface breaking pores/defects, while the RUS approach produces a higher value relative to the XCT approach. Based on the XCT images and the acoustic microscope results, the porosity/defects reside mostly in the internal region of the coupons. The impact of surface finishing and material removal may increase the volume fraction of the pores/defects between the value estimated from the XCT voxel calculation approach on the unmodified coupons and the RUS method on the smooth/polished samples. However, further work is needed to confirm this observation.

Table 13. Estimated Porosity in the 316L DED Coupons Using Different Approaches.

Method	INL-DED-1 (%)	INL-DED-2 (%)
XCT Image	1.64	3.83
Archimedes	1.78	2.48
RUS	1.45	4.53

2.2 Wall Thickness Measurements on DED 316L Cylinder

This section describes the approach to apply a frequency analysis of the reflected ultrasonic amplitude spectrum to measure the wall thickness variations in a DED 316L cylindrical component. Due to the surface roughness of the component, traditional pulse-echo methods experience large signal loss and low signal-to-noise ratios (SNR), making measurements of internal defects and wall thickness impractical or impossible. The thin wall of this specimen also necessitates other methods as there is not enough separation in the acoustic response between the front and rear wall interfaces in the specimen for traditional ToF measurements at frequencies that are low enough to pass through the rough surface. The objective of this effort is to assess the ability of the reflected ultrasonic amplitude spectrum frequency analysis method to overcome the surface roughness conditions so that wall thickness and defect evaluations can be performed.

The following provides a brief overview of the ultrasonic-based wall thickness measurement methodology, a description of the DED 316L cylindrical component, a summary of the approach used to perform the wall thickness measurements, a discussion of the data collection and analysis performed to acquire the wall thickness values, and a review of the results.

2.2.1 Overview of the Method of Frequency Analysis Used for Thickness Measurements

The method to measure the geometric wall thickness uses a continuous wave ultrasonic signal to generate reflected signals that contain information on the reflectance and transmittance characteristics of the component. This approach leverages the facts that an ultrasonic signal

has a certain fraction of energy that is either reflected or transmitted at interfaces where acoustic impedance changes occur and that specific frequencies will set up resonances within the specimen. With a broadband ultrasonic signal, the frequency (or frequencies) that matches the resonance condition will pass through the material virtually unimpeded, meaning that those specific frequencies will be absent (or diminished) in the reflected spectrum. As a result, the energy that is reflected back to the transceiver will lack frequency components of the transmitted sound, which can be observed as depressions in the frequency spectrum. Variations of this approach have been developed to measure coating thicknesses, measure inter-layer thicknesses in multi-material components, and measurement of elastic properties of thin layer (Krautkrämer 1990, Haines 1978, Lavrentyev 2021).

In the case of the application described herein, the test sample is submerged in water, and an ultrasonic wave is transmitted through the water and interacts with the specimen wall. A portion of ultrasonic energy—with a half-wavelength multiple of the wall thickness—will be transmitted through the plate and not be detected. In effect, the plate becomes a 1/2-wave filter, and by measuring the filtered frequency, the plate thickness can be calculated using the following relationships:

$$t = \frac{n \cdot \lambda_R}{2} \; for \; n = 0, 1, 2 \ldots. \tag{5}$$

$$\lambda_R = \frac{c}{f_R} \tag{6}$$

where t = Material thickness
λ_R = Wavelength at resonant frequency
f_R = Resonant frequency
c = Speed of sound in the material

By applying a Fast Fourier Transform (FFT) analysis to the reflected ultrasonic signal, the amplitude of the reflected frequencies can be generated. At the frequences corresponding to the resonant condition, reductions, or dips, are observed in the FFT. An example of FFT analysis is shown in Figure 21 for a 3 mm thick plate of 316L wrought SS material. The specific frequency information can then be used in Equations 5 and 6 to obtain the material thickness.

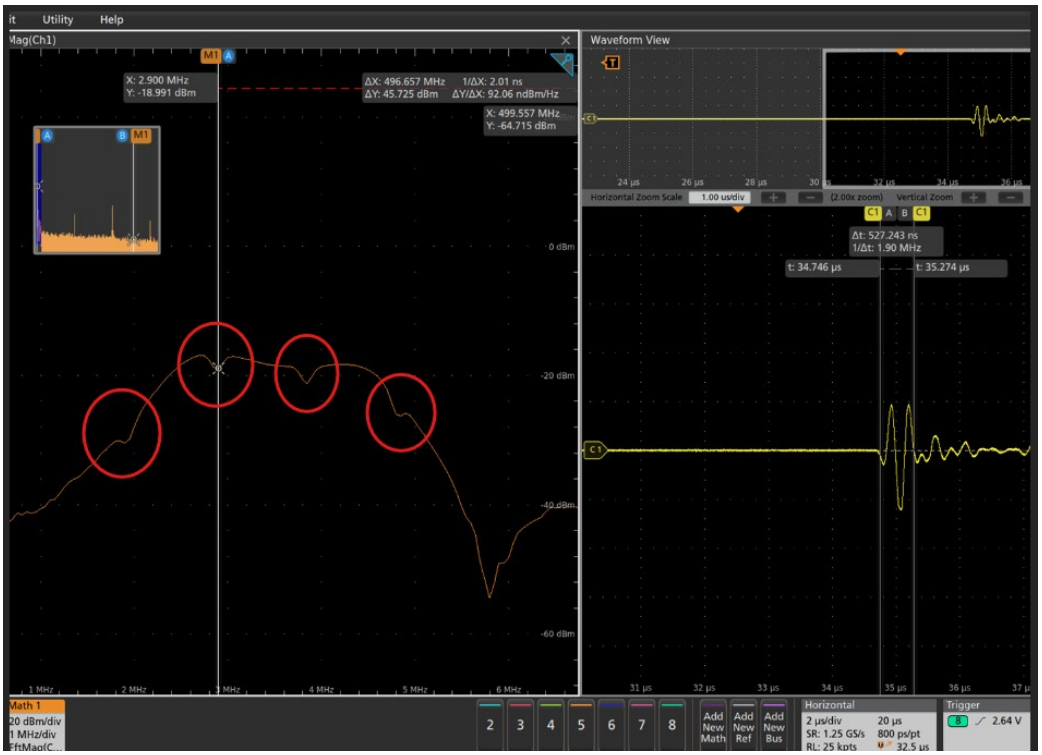

Figure 21. Example FFT Analysis (left image) of the Reflection Signal from a 3 mm Thick Plate Highlighting the Amplitude Reductions at Specific Frequencies

2.2.2 Description of the DED 316L Cylinder

The SS316L cylindrical component used in this evaluation was manufactured with a powder DED additive manufacturing method. The DED method applies a fine powder that is sprayed out of a nozzle and fused continuously with a plasma arc to steadily build up the final desired shape of the component. As with most additive manufacturing techniques, the process produces a part that has pronounced layer lines (or ridges and valleys) on the surface in addition to roughness from the individual powder particles. A picture of the cylinder is shown in Figure 22, with the circumferential ridges visible. Surface roughness scatters incident and reflected sound; the resulting ridges and overall surface condition had a significant impact on the ultrasonic SNR. In addition, the cylinder was intended to be circular; however, due to residual stress from the build process, the final shape had a slight ovality. The rough dimensions of the cylinder are: height is approximately 190 mm, outer diameter is nominally 135 mm, and wall thickness is approximately 2.4 mm (measured from the peaks of the ridges). The beginning of the build is the right edge (bottom) of the cylinder as shown in Figure 22 and a transitional, or tapered, region in the outer diameter is visible for the first ~15 mm of the build process. Beyond the transitional region, the outer diameter is nominally constant, save for the slight ovality.

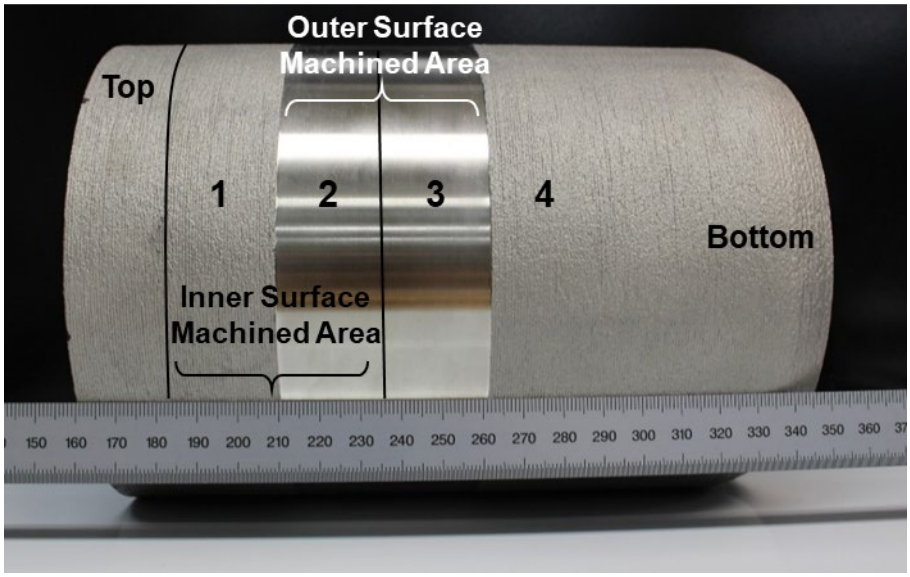

Figure 22. Photograph of the DED 316L Cylinder Laying Horizontal. The Post-Fabrication Machined Surface is Seen in the Center Part of the Image.

The surface roughness features caused by the powder DED fabrication process inhibit the reflectance and transmittance of ultrasonic signals from the component. To evaluate the impact of the surface features, mechanical removal of the ridges was performed using a lathe on both the inside and outside surface. Four (4) regions (as indicated in the figure) were created along the axial height of the component corresponding to:

1) inside smooth – outside rough,
2) inside smooth – outside smooth,
3) inside rough – outside smooth,
4) inside rough – outside rough (as-manufactured).

The three machined regions are approximately 25 mm in length along the axial direction as shown in Figure 22. The remainder of the cylinder surface falls into the 4th zone. In addition, a Dremel tool was used to score the inside surface within region 2 to provide a simulated surface defect.

2.2.3 Ultrasonic Scanning and Data Collection System

Generating a thickness map over a large area of the DED 316L cylinder was of particular interest due to the potential variability in wall thickness created by the stacked layers in the build process. To this end, scanning of the cylinder was performed using a rotary scanner designed for scanning the inner surfaces of reactor vessel head penetrations. A special adapter was designed to configure the scanner for circumferential and axial scanning of the outer surface of the cylinder. The scanner sat on the component and was rotated around the coincident central axis as shown in Figure 23. The adapter was placed on the bottom of the cylinder to allow for the upper region to be examined. An ultrasonic probe was placed on the arm of the scanner pointing in towards the outer surface of the specimen. By accurately controlling both the circumferential and vertical motion, the scanner can position the probe over the entire exposed outer surface of the component, although the adapter prevented scanning the bottom ~53 mm of the cylinder, including the transition zone. As shown in Figure 23, the component was placed in water to provide ultrasonic coupling. The reflected signal was detected by the ultrasonic probe in a pulse-echo configuration. The scanner was driven by an in-house motor controller. The probe position was controlled and recorded by a Zetec Dynaray. The Dynaray was driven by the Zetec UltraVision software, and this system allows for exporting of the raw wave forms and positional data for post-process analysis.

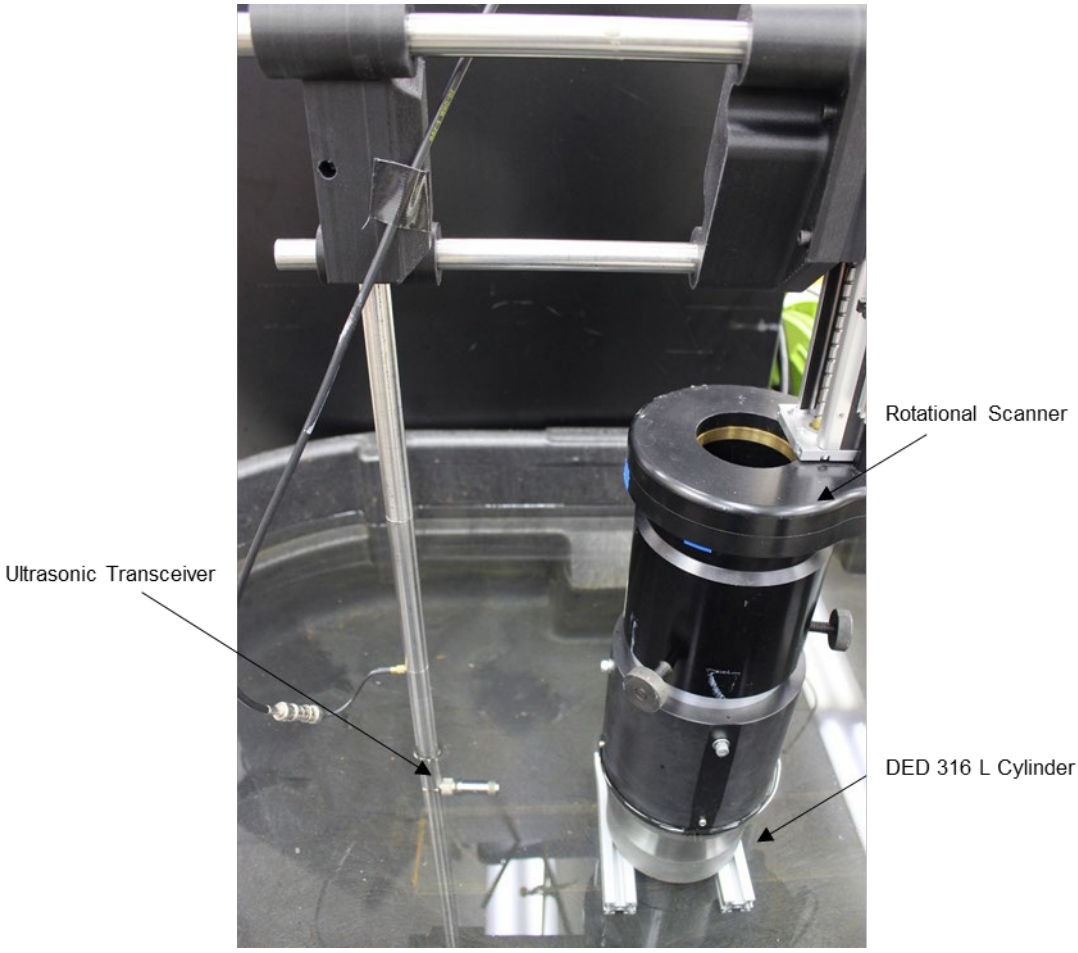

Figure 23. Rotational Scanner and Probe Setup for the Examination of the DED 316L Cylinder

Various UT probes spanning a range of frequencies, focal depths, and spot sizes were evaluated to assess their performance in this application. The probe selected had a center frequency of 10 MHz. Due to attenuation and scatter, the received sound was centered at about 7 MHz. Loss of high frequency components due to attenuation is common in ultrasonics and is compensated for by broadband probes and electronic filters. This probe had a 19 mm diameter aperture and was designed to be focused at 100 mm in water. Data was collected every half degree around the cylinder and with 0.1 mm axial resolution.

2.2.4 Preliminary Wall Thickness Results

The raw data from the UltraVision Software was reconstructed in Python for post processing using an algorithm that used the frequency spectrum to identify the cylinder wall thickness. An FFT was performed to obtain the spectrum of each waveform at every measurement location in the scan. Each FFT was normalized to have a max of unity (1), and a smoothing function was used to eliminate noise that would interfere with frequency depression-finding algorithms. Both the smoothing function and the depression-finding function were optimized through an iterative process. High and low frequency-depression regimes were identified during the data processing that were sensitive to different geometric features. The wall thickness results for the high frequency depressions are shown in Figure 24. The horizontal axis represents the circumference of the cylinder. Results show that the information from the high frequency regime give clean signals over the regions of the cylinder that had their outer surface machined smooth. The rest of the image is dominated by noise, as the higher frequency sound was more strongly scattered by the rough outer surfaces. The circled indications are two notches ground into the inner surface with a Dremel tool for defect detection evaluation.

The figure illustrates two important results. The first is that, due to the ovality of the pipe and the post machining process making a round outer surface, there is a slight wall thickness variation around the circumference that clearly shows up in the scan. For example, in region 3, the wall thickness varies from about 1.8 mm to 2.0 mm, but in region 2 there is less variation in wall thickness because both the inner and outer surfaces were machined. The gradual changes in wall thickness around the cylinder demonstrate that the method is sensitive to small thickness variations (<0.1 mm). Second, wall thickness measurements were possible in region 3, where the outer surface is smooth but the inner surface is rough. However, results in region 1, where the inner surface is smooth but the outer surface is rough, were dominated by noise. Indeed, the results from regions 1 and 4 were identical (1.90 ± 0.07 mm and 1.90 ± 0.08 mm, respectively) in spite of the inner surface of region 1 having been machined. With a rough outer surface, sound is scattered and attenuated twice—once upon entering the material and again upon exiting. This, coupled by the higher frequencies being more susceptible to scatter and attenuation, resulted in noisy spectra and poor wall thickness results in regions 1 and 4.

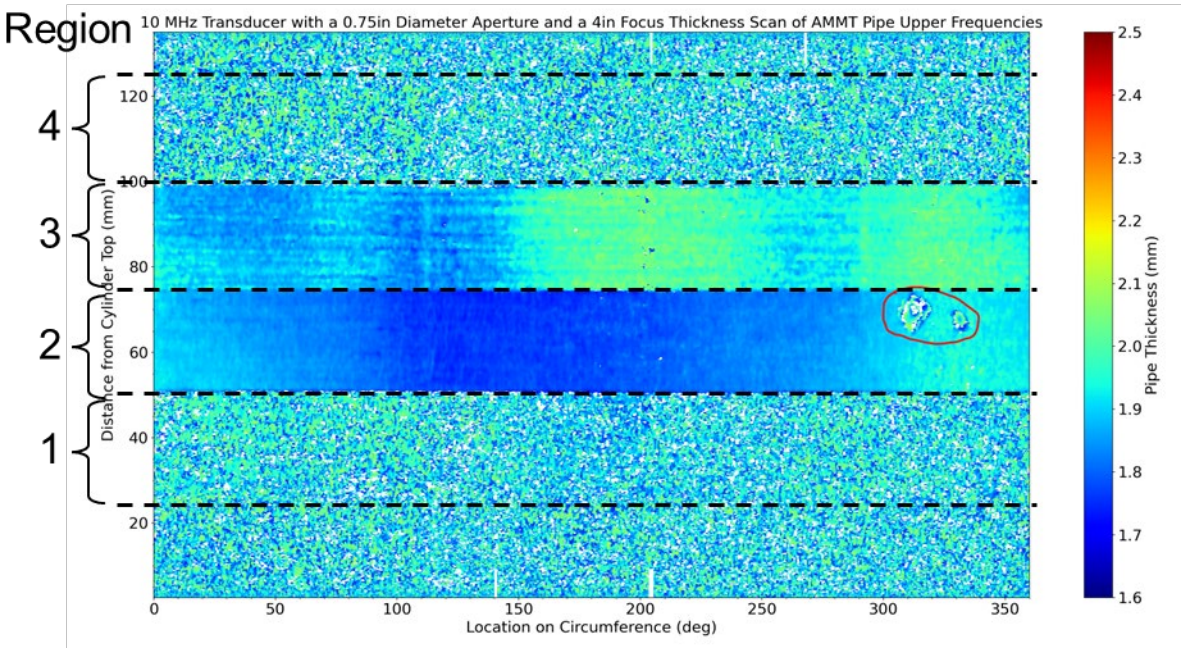

Figure 24. Wall Thickness Contour Map from the FFT Post-Process Using the High Frequency Depression Regime.

Figure 25 provides the wall thickness results from the low frequency regime. As stated above, the lower frequencies are less scattered and attenuated by the surface roughness, so there should be less noise in the regions that have rough outer surfaces. However, the lower frequency spectral dips are typically less reliable for making thickness measurements because of the inverse relationship between the thickness and the frequency. Thus, the low frequency analysis tended to have more measurement variation and had more regions where the analysis did not give a result; these regions are shown as white pixels in the image and represent missing data.

Similar to Figure 24, Figure 25 shows variations in the wall thickness measured around the circumference, particularly in region 2. However, the lower frequency analysis also shows thickness results in regions 1 and 4, where the outer surfaces were not machined smooth. The average wall thickness in regions 1 and 4 were 1.94 ± 0.09 mm and 2.03 ± 0.10 mm, respectively. Although these values are not statistically different, the lower average in region 1 is consistent with the fact that the wall was thinner because the inner surface of that region was machined smooth.

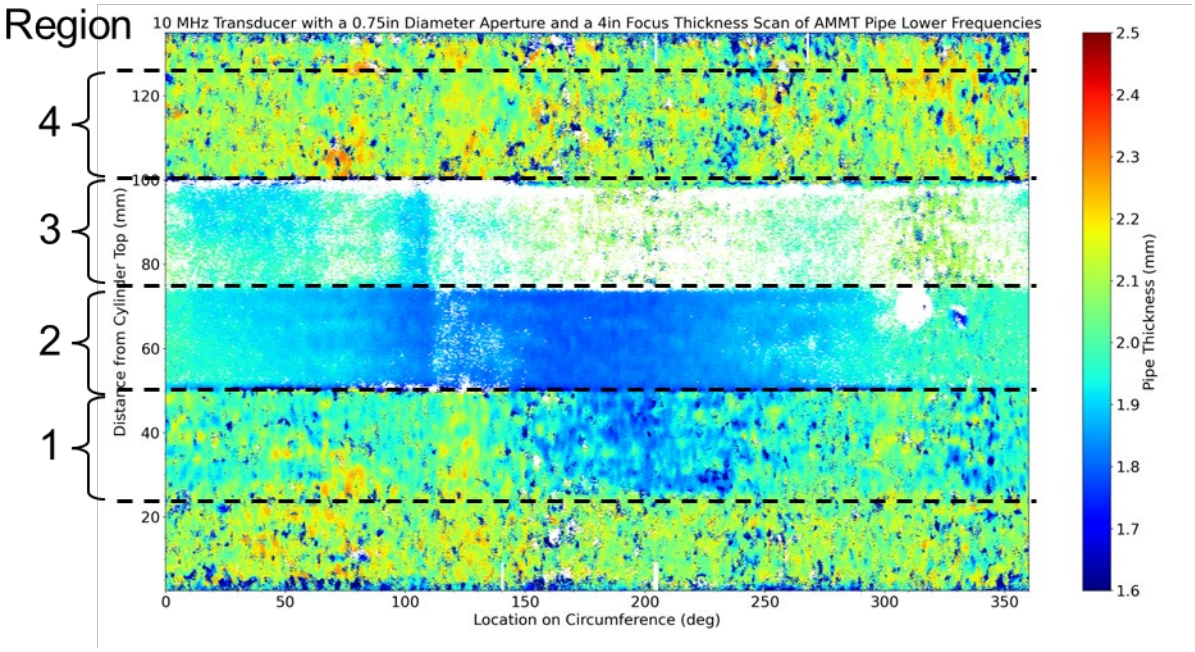

Figure 25. Wall Thickness Contour Map from the FFT Post-Process Using the Low Frequency Depression Regime.

The results for the two frequency depression regimes were combined using a max of each image to yield the final wall thickness contour map shown in Figure 26. The average ± standard deviation thicknesses of each region are (in mm):

1) 1.97 ± 0.07
2) 1.86 ± 0.05
3) 1.97 ± 0.06
4) 2.05 ± 0.07

The results agree with expectations. The thickest region was measured to be region 4, where no machining was done, while the thinnest region was region 2 where both the inner and outer surfaces were machined. Regions 1 and 3 each had one surface machined, and the results of those regions were consistent. The relatively high standard deviation of region 2 (the region with the least noise) compared to that of region 4 was due in part to the ovality of the cylinder. Considering only the section between 150-250 degrees, the thickness of region 2 was 1.81 ± 0.03 mm, which is below the overall region 2 average (the cylinder was slightly thinner in this location) and has less measurement variation.

Recall that the thickness of the cylinder was measured to be about 2.4 mm prior to machining, but this was done with calipers and therefore represents the maximum thickness due to the roughness peaks. The ultrasonic approach will naturally incorporate some spatial averaging due to the finite size of the sound field (i.e., roughness “valleys” will be included along with the peaks), leading to a lower measured value than that obtained with calipers.

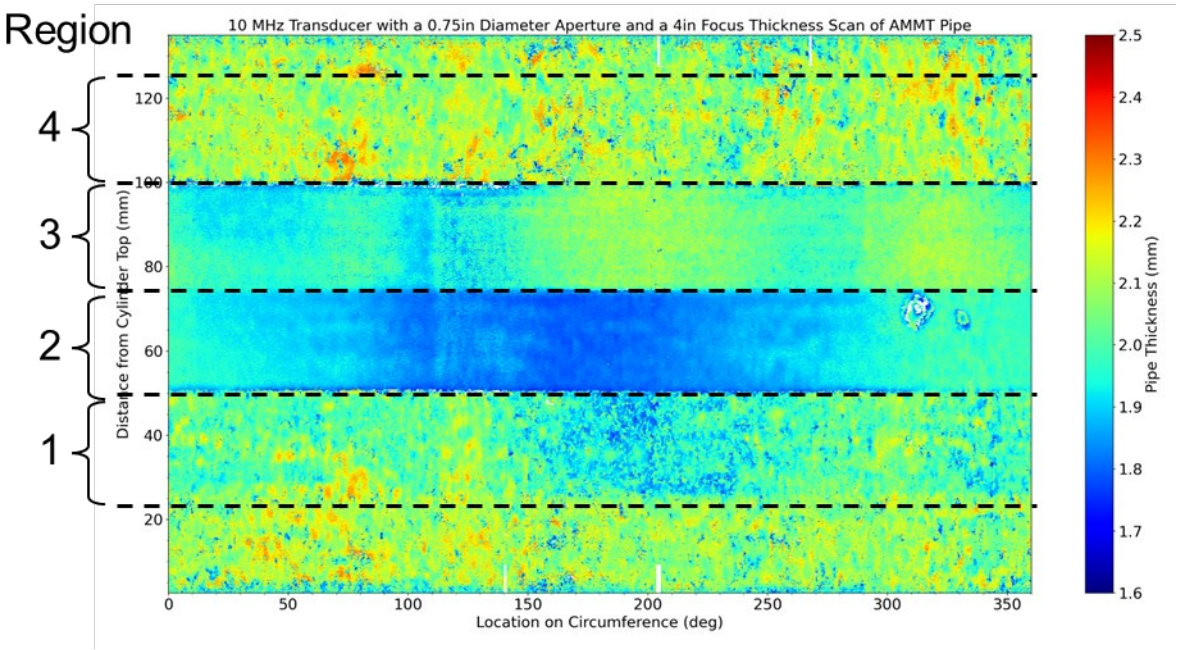

Figure 26. Final Wall Thickness Contour Map from the FFT Post-Processing Method

2.2.5 Comparison with Destructive Examination Measurements

Upon completion of the NDE wall thickness measurements, a destructive examination plan was developed to obtain wall thickness measurements, perform metallographic examinations of the microstructure, and perform residual stress measurements. The sectioning plan is shown in Figure 27. The component was sectioned into four (4) 90-degree segments, and a 4 mm wide strip was removed at 0º, 90º, 180º, and 270º for further examinations, including wall thickness, scanning electron microscopy, and X-ray diffraction for residual stress.

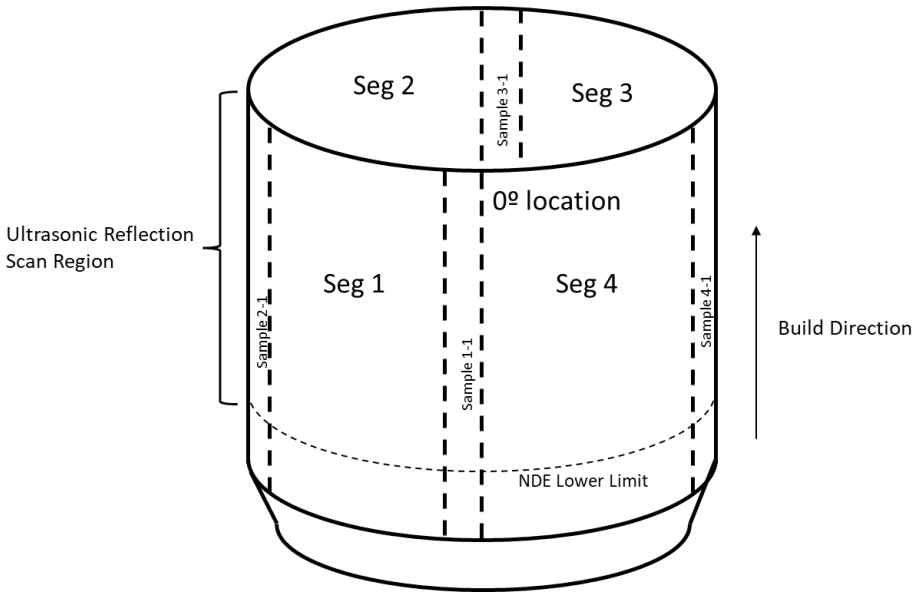

Figure 27. Sectioning Plan for the Destructive Examination of the DED 316L Cylinder

Samples 1-1, 2-1, and 3-1 were used to measure the wall thickness along each sample for comparison to the ultrasonic scan results using an optical approach. Sample 4-1 was sent out for further microstructural examinations and residual stress measurements. These examinations will be reported separately.

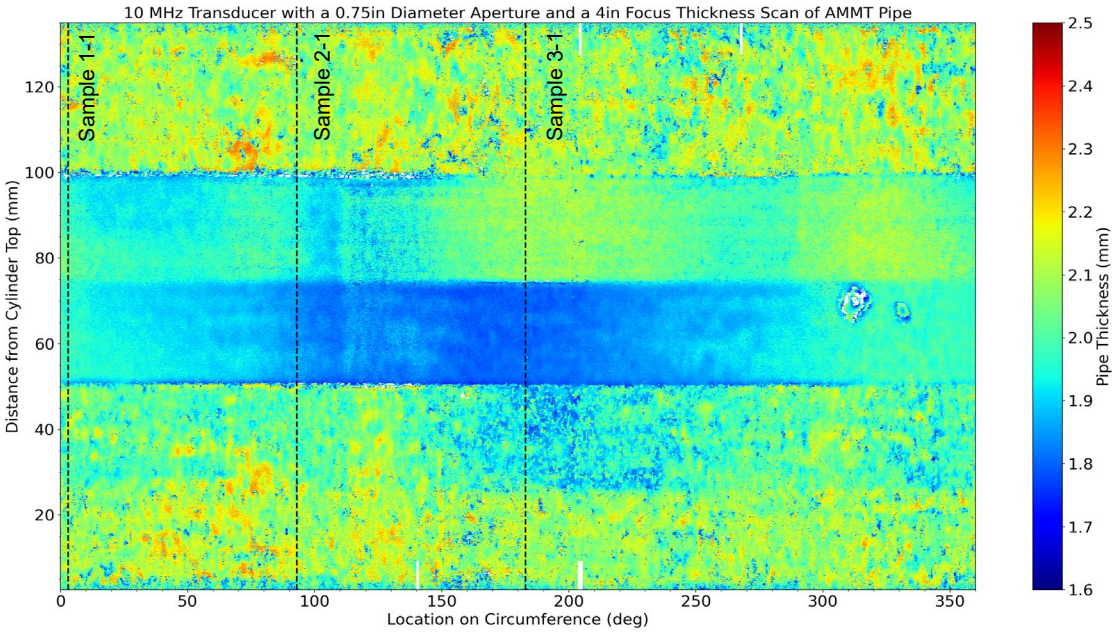

Figure 28. Location of Destructive Examination Measurements of Wall Thickness For Comparison to the Ultrasonic Reflection Results

The location of Samples 1-1, 2-1, and 3-1 with faces at approximately 3º, 93º, and 183º degrees are shown as vertical black dotted lines in Figure 28. Each sample was set up in an X-Y scanner with a high-resolution camera and a Canon Macro 180 mm f/3.5 zoom lens. The camera was set high over a specimen, the specimen was placed on its edge, and the specimen was backlit to better differentiate the edge. A series of pictures were taken along the length of the sample and stitched together to help eliminate parallax. An example of the optical wall thickness measurement setup is shown in Figure 29. These pictures were imported into Python, and the Open CV library was used to find the edges. With a known distance per pixel gathered from a ruler in the images, the thickness of the segment at every horizontal pixel position was generated. The optical scan of the samples produced a wall thickness value as a function of position along the axial length for comparison to the ultrasonic reflection measurements. As observed in Figure 29, Sample 1-1 exhibits significant bow cause by the presence of residual stress. This lack of straightness was observed to various degrees in all 4 samples.

Figure 29. Photograph of the Optical Scan System Used to Obtain the Wall Thickness from the Destructive Examinations for Sample 1-1

The wall thickness measurements from the optical method are compared to the ultrasonic reflection method in Figure 30, Figure 31, and Figure 32. Each figure contains the following: (top) optical silhouette for destructive thickness measurement, (middle) wall thickness along axial length from ultrasonic reflection and optical methods, and (bottom) deflection from straightness. In all three comparisons, good agreement is observed between the nondestructive method (ultrasonic reflection) and the destructive method (optical). There are some areas where some differences are noted, and further study is needed to ascertain the cause of these differences.

The complicated surface features from the powder DED fabrication process can be seen in both data sets as local variations around a mean wall thickness value. In the regions where the surface features were removed by machining (Regions 1, 2 and 3 in Figure 30), the variability in the wall thickness is reduced. The results for the wall thickness measurements indicate that the surface feature heights are in the range of 0.1 to 0.2 mm on both inner and outer surface. The surface features, especially on the outer surface, influence the wall thickness measurements by scattering the incoming ultrasonic energy and reducing the reflected wave amplitude.

Finally, all three samples exhibit deviations from straightness that was observed in the destructive examinations. These deviations reach ~6 mm over the 175 mm length in Sample 3-1 and indicate some level of residual stress was present in the DED 316L cylinder. Further work is needed to understand the impact these deviations on the integrity of the component.

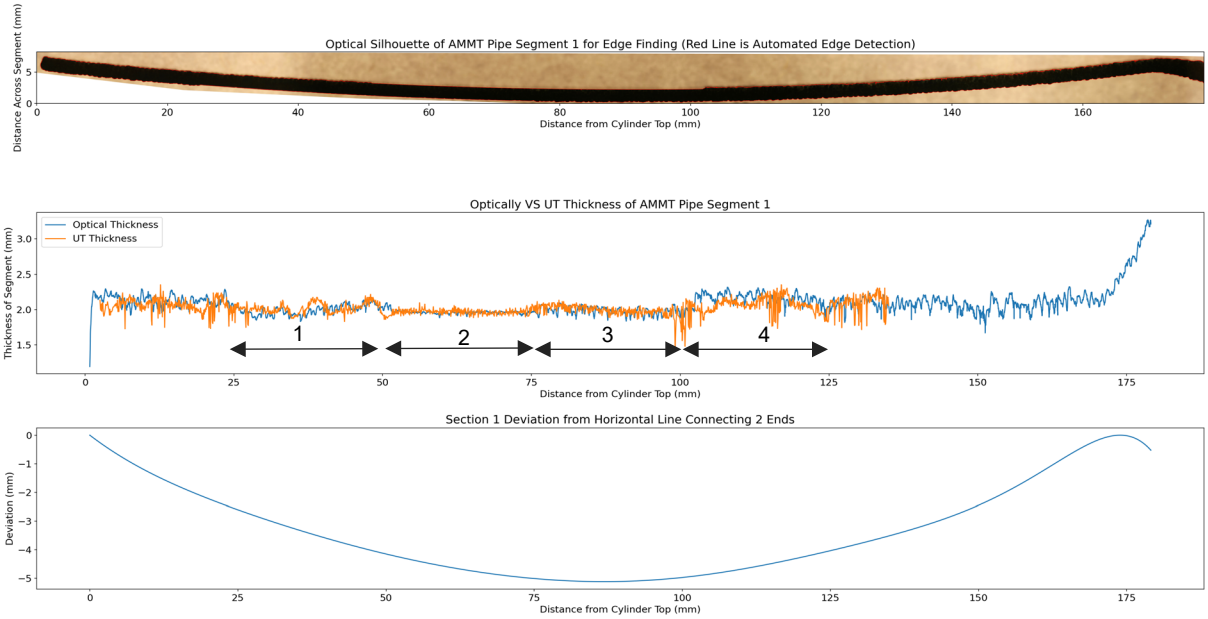

Figure 30. Comparison of Ultrasonic Reflection Wall Thickness Measurement with Values from Destructive Optical Scan Measurements for Sample 1-1.

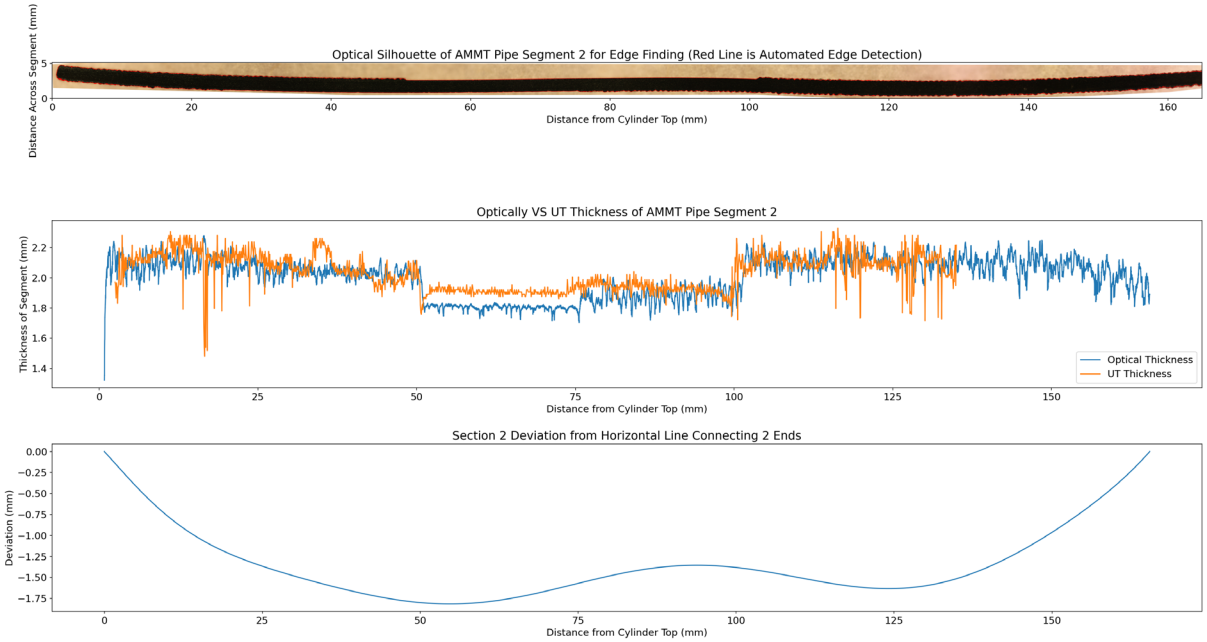

Figure 31. Comparison of Ultrasonic Reflection Wall Thickness Measurement with Values from Destructive Optical Scan Measurements for Sample 2-1.

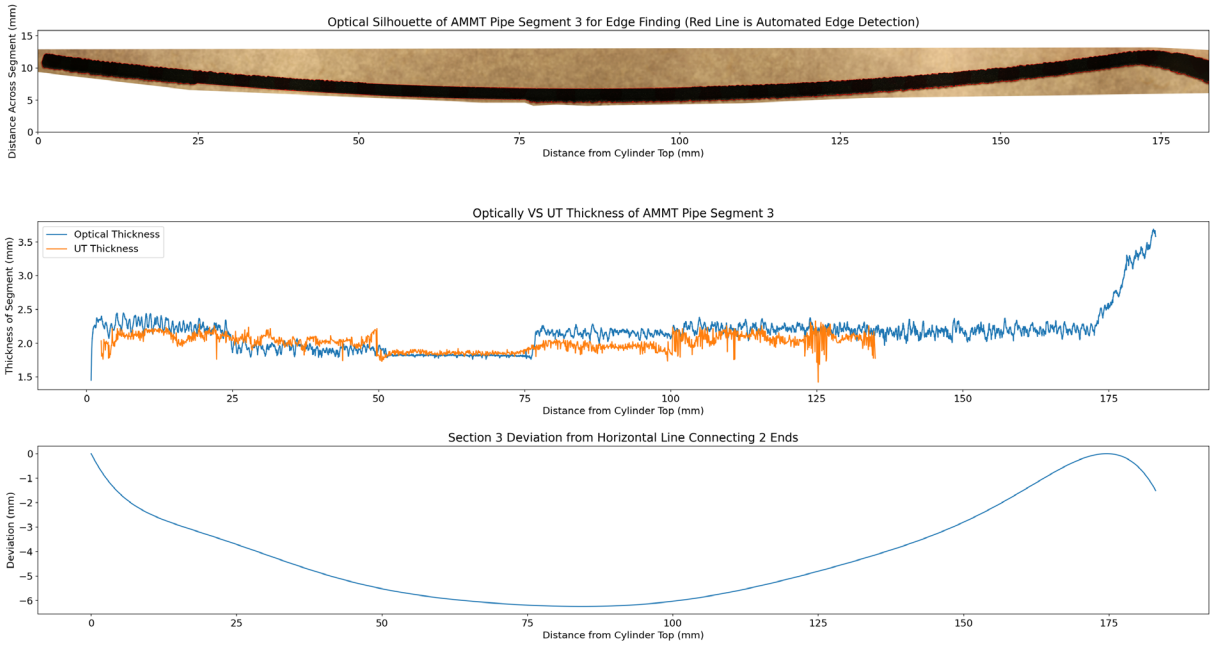

Figure 32. Comparison of Ultrasonic Reflection Wall Thickness Measurement with Values from Destructive Optical Scan Measurements for Sample 3-1.

The preliminary results from the ultrasonic spectrum analysis method demonstrate the potential to use this method to investigate the geometry conformity and presence of defects in components made with DED. Preliminary results suggest that this method can be applied to real world components, but the issue of surface finishing will need to be addressed. The data show that the method is more sensitive to the outer surface condition than it is to the inner surface, especially at the higher frequencies needed to resolve finer details. However, the work did not evaluate how smooth the surfaces actually need to be to obtain useful data.

Future work will determine the degree of and locations where surface finishing will be required in order to obtain robust data while minimizing post-build processing, which can add considerable time and cost to component production. Exploring the use of an ultrasonic chirp over a sweep of frequencies can be done to better detect and isolate the frequency depressions. Another goal is to detect and resolve internal defects. While the frequencies used herein were sensitive to large inner-surface defects, it is unclear whether they would be useful for resolving small internal defects. Further studies are needed on a component with known internal fabrication defects to better understand the ideal ultrasonic parameters for detecting such flaws. For example, the frequency sweep approach may increase the frequency range obtained by the probe to obtain better spatial resolution and interrogate the interface between material layers. Advanced ultrasonic methods can also be tested for defect detection, such as phase coherence imaging or full matrix capture. Finally, future work can explore the ability to precisely measure the ultrasonic shear and longitudinal velocities in these thin-walled components, which will enable nondestructive calculation of mechanical properties. For example, a map of the mechanical properties could be produced to show locations of residual stress and help predict potential locations of future defect formation.

3.0 INL Imaging-Based Methods

In FY24, the NDE work at Idaho National Laboratory (INL) for the AMMT program focused on building upon previous efforts (Chuirazzi et. al.,2023) to further explore and demonstrate a variety of NDE techniques within the AM application space. Techniques included X-ray CT and diffraction (XRD), neutron CT and diffraction, LIT, and PAS. This year's work scope continued previous nondestructive investigations of AM samples to inform the long-term goal of creating a multimodal workflow to nondestructively investigate as-fabricated component scale specimens to ensure quality and safety for use in commercial reactor applications.

3.1 X-ray Computed Tomography and Diffraction of 316L DED Specimens

3.1.1 X-ray Computed Tomography

Previous FY23 work focused on examining a series of 6 DED SS316L samples with XCT. The samples were intentionally crafted with a variety of fabrication parameters in an effort to correlate fabrication parameters with defect generation. However, after this data, shown in Figure 33, was analyzed, it was concluded that there were insufficient data points to draw strong conclusions between the fabrication parameters and the defects induced by them. Calculations were made to determine the appropriate settings for specific energy and powder density. Based on these calculations an additional 20 samples were fabricated with the goal of performing XCT to quantify the porosity in each sample. The parameters of the new samples can be found in Table 14.

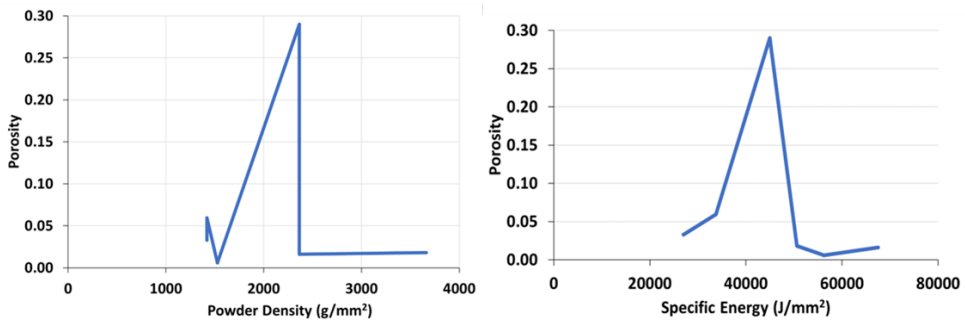

Figure 33. Initial results of (left) porosity as a function of powder density and (right) porosity as a function of specific energy.

Initial measurements were undertaken on the new batch of samples, but these samples were slightly larger than the previous samples. The larger sample size required imaging stitching to image the entirety of the samples while maintaining the spatial resolution used for the previous samples. This doubled and, in some cases, even tripled the scan time compared to the previous samples, making it difficult to scan all samples in a timely manner.

Table 14. Fabrication parameters of additional DED 316L samples.

Sample ID	Specific Energy (SE) [J/mm^2]	Powder Density (PD) [g/mm$^{2]}$	Laser Power [J/s]	Hatch Linear Feedrate [mm/s]	Powder Feedrate [g/min]
1	4.50E+04	2364.456	200	6.35	10.51
2	2.70E+04	1418.674	200	10.58	10.51
3	5.62E+04	1527.56	250	6.35	6.79
4	3.37E+04	1418.674	250	10.58	10.51
5	6.75E+04	2364.456	300	6.35	10.51
6	5.06E+04	3661.42	300	8.47	21.7
7	4.50E+04	2.36E+03	200	6.35	10.51
8	4.08E+04	3.67E+03	200	7.00	18
9	2.14E+04	1.50E+03	150	10	10.51
10	2.38E+04	1.08E+03	150	9	6.79
11	7.87E+04	2.36E+03	350	6.35	10.51
12	7.87E+04	4.88E+03	350	6.35	21.7
13	5.62E+04	2.36E+03	250	6.35	10.51
14	3.57E+04	1.50E+03	250	10	10.51
15	3.97E+04	1.08E+03	250	9	6.79
16	6.75E+04	2.36E+03	300	6.35	10.51
17	4.76E+04	1.67E+03	300	9	10.51
18	5.44E+04	9.24E+02	400	10.5	6.79
19	5.44E+04	2.95E+03	400	10.5	21.7
20	3.57E+04	2.38E+03	150	6	10

However, INL partnered with Oak Ridge National Laboratory (ORNL) to license the Simurgh reconstruction code (Ziabari 2022). This machine learning based algorithm reconstructs 3D volumes with significantly less 2D projections than required with traditional algorithms. The implementation of Simurgh for this project has reduced data acquisition times by roughly 90%, enabling all samples to be imaged during FY24. In addition to data reconstruction, Simurgh also employs image processing algorithms to reduce noise in the data. An example of the Simurgh output is shown in Figure 34. Using Simurgh and some custom data processing codes developed at INL, a workflow was created to quickly image the specimens and reduce the data collected. Due to Simurgh's implementation, all samples have been imaged and undergone data reduction at the writing of this report.

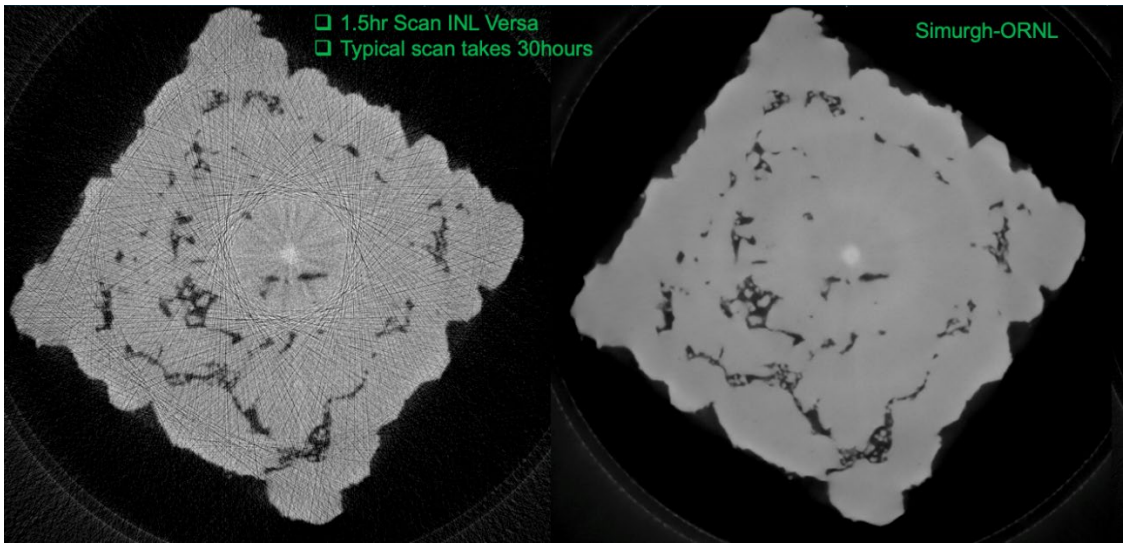

Figure 34. Cross-sectional 2D views of XCT reconstructed volumes for the same sample of (1) data reconstructed with the standard commercial software and (2) the Simurgh algorithm.

Additionally, two of the previously examined samples were sent to PNNL to undergo RUS measurements. The goal of this collaboration is to compare XCT and RUS measurements to lay the foundation for a multimodal examination framework. This could ultimately enable multi length scale examination models that could help to qualify AM reactor components for commercial use. The ultrasonic inspection of these samples is contained in Section 2.1.3

3.1.2 X-ray Diffraction

After the initial round of DED samples was examined with XCT, samples exhibiting high porosity were subjected to X-ray diffraction for residual stress measurements. The goal of these measurements was to observe if the residual stresses introduced during fabrication varied spatially across the sample and to correlate the residual stresses to porosity. X-ray diffraction patterns and single peak measurements were taken and ultimately used to derive residual stress measurements. The series of measurements collected on one specimen are shown in Figure 35.

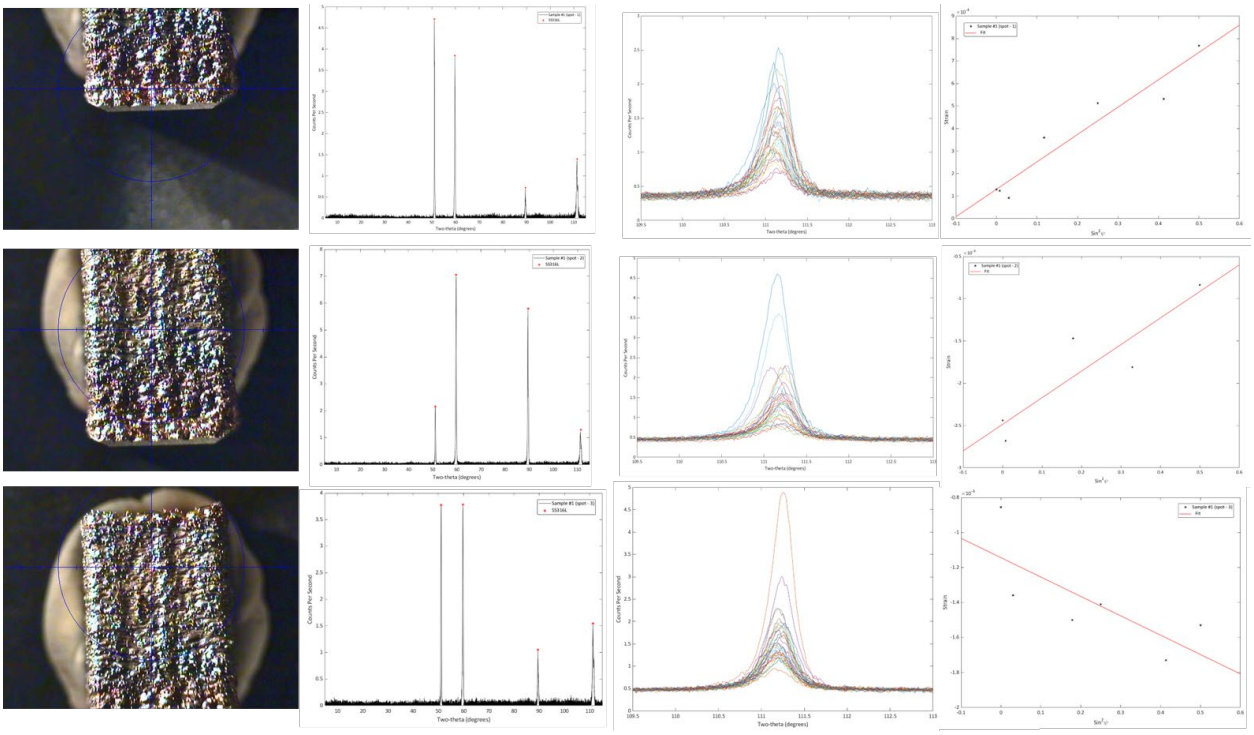

Figure 35. XRD measurements taken at three different locations on a DED SS316L sample. Measurements were taken near the top (first row), middle (second row), and bottom (third row) of the sample. (Left) An optical image showing the measurement location on the sample. (Middle Left) XRD patterns and (Middle Right) single peak measurements are used to derive the (Right) residual stress measurements results.

The sample shown in Figure 35 was determined to have tensile residual stresses that decrease from the top of the sample to the middle of the sample before changing to a compressive stress near the bottom of the sample. Near the top of the specimen a residual tensile stress of 197.8 MPa was measured, decreasing to a value of 51 MPa near the middle. At the bottom of the sample a residual stress of -18.0 MPa indicates a compressive stress at this position.

Additional samples will undergo XRD to get a more comprehensive characterization of the residual stress patterns created by the DED manufacturing process. The goal of XRD measurements will also be to complement other NDE techniques to produce a clear correlation between fabrication parameters and defect generation. Instrumentation upgrades scheduled for the end of FY24 should drastically increase the throughput of these measurements.

3.1.3 Future Work and Outlook

During FY24, work started during the previous fiscal year was significantly advanced and augmented. However, outstanding tasks remain. Future work on this effort will entail full analysis of the XCT results. Once accomplished, the porosity for each fabrication parameter will be correlated to help optimize DED fabrication. Additionally, samples of interest will undergo further XRD measurements to correlate porosity to induced residual stress as well as correlating the relationship between residual stress and the fabrication parameters themselves. Upon completion of the XCT and XRD measurements, a peer-reviewed journal manuscript may be submitted on this work, pending the results of the final data.

3.2 Neutron Imaging and Diffraction

Neutron computed tomography and residual stress measurements on DED SS316L had previously been acquired at ORNL as part of a now defunct effort. During FY24, this data was reduced, analyzed and interpreted to successfully complete the M3 milestone of this work package, which was to write and submit a journal publication on the results of neutron investigation into the DED SS316L material. While this FY24 effort primarily dealt with data analysis and interpretation, it provides a clear demonstration for the usefulness of nondestructive neutron examination techniques to characterize additively manufactured parts.

In this work, a total of 6, 8 mm × 8 mm × 10-20 mm rectangular blocks of SS316L were fabricated with DED. Hatch spacing and track overlay were varied between the samples to discern their effect on the final build. Once fabricated, these parts were examined using nCT at the CG-1D beamline and neutron diffraction at the HB-2B beamline, both at ORNL's High Flux Isotope (HFIR) reactor.

Two samples, one with 25% overlap ratio and the other with 50% overlap ratio, underwent nCT. Once collected, the data was segmented and connected component analysis was performed on the pores. While the 25% overlap ratio sample only had 0.002% porosity, the porosity of the 50% overlap sample was even lower with an observed porosity of only 0.0008%. In the 25% overlap sample, a total of 6 pores were able to be resolved with the effective spatial resolution of 37 µm/voxel, while only 4 pores were measured in the 50% overlap sample. Table 15 shows the results of quantitative image processing on the pores, whereas Figure 36 shows CT images for the samples.

Table 15. Results of Connected Component Analysis on Pores.

Sample with 25% overlap ratio			**Sample with 50% overlap ratio**		
Volume (µm3)	Equivalent Diameter (µm)	Surface Area (µm2)	Volume (µm3)	Equivalent Diameter (µm)	Surface Area (µm2)
6.1E+06	220	160000	5.0E+05	98	26000
9.0E+06	250	210000	8.8E+05	110	39000
1.7E+07	320	35000	1.5E+06	140	61000
2.1E+06	150	75000	3.6E+06	190	110000
5.0E+05	98	25000			

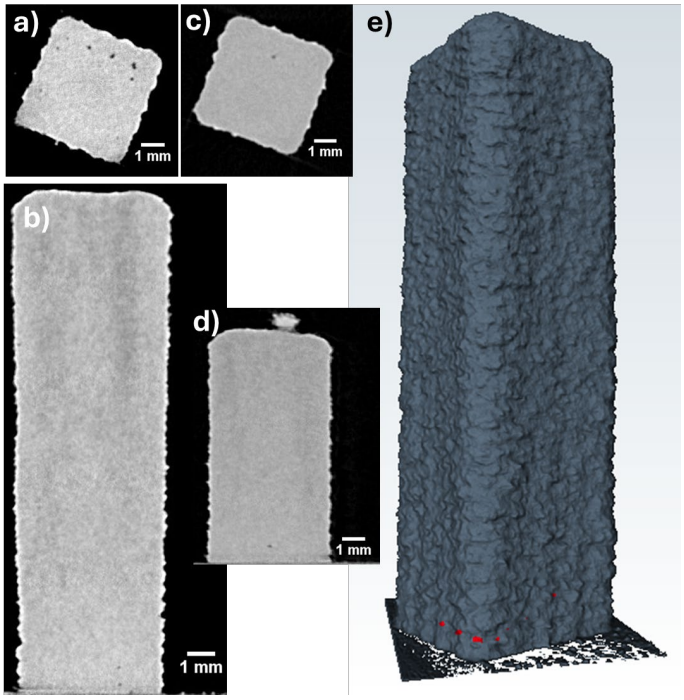

Figure 36. Two-dimensional cross-section images (slices) of the three-dimensional tomographs for (a) and (b) 25% overlap and (c) and (d) 50% overlap samples. A 3D rendering of the 25% overlap sample (e) shows pores (in red) relative to the rest of the sample.

Residual stress measurements, utilizing a neutron wavelength of 1.5323 Å, were conducted on all 6 samples. These measurements showed residual stress to be higher in the middle of the sample compared to the bottom and the top along the build direction. More residual stress hotspots were present in samples with larger hatch spacings (lower overlap ratios). The results of the averaged residual stress of each z position are displayed in Figure 37. It is noticeable that at the bottom of the deposited samples, σ_z is more compressive than the in-plane stress components (σ_x and σ_y), but this difference disappears for layers further away from the base plate. In addition, all samples show fewer tensile stress hotspots in σ_z than in σ_x and σ_y. Because the z- dimension is significantly larger than the x- and y- dimension, it may be the case that the effects of remelting during the build process along the build direction would be smaller than the x- and y- dimensions.

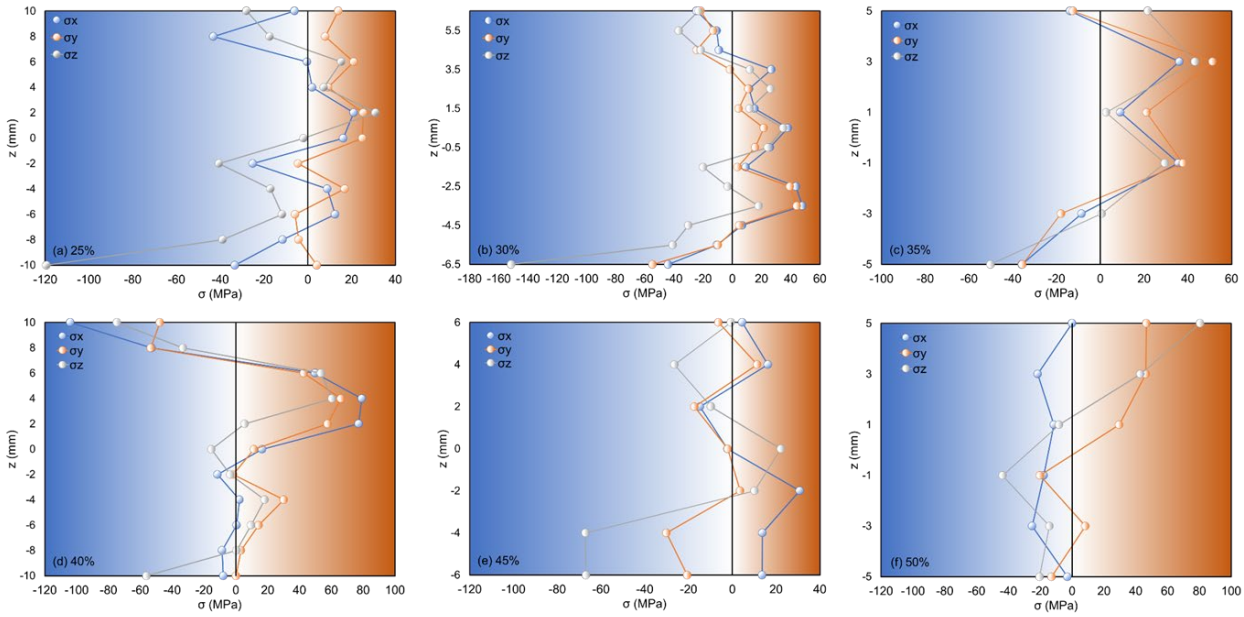

Figure 37. Plots of Averaged Residual Stress of Each Z Position For All Samples.

These neutron measurements showed porosity primarily concentrated at the base of the deposited materials, which is consistent with previous observations in the literature (Pang 2019). Additionally, lowering the hatch spacing (increasing the overlap ratio) resulted in a lower porosity, which may be due to large thermal fluctuations across the build plate at the beginning of the sample fabrication process. Cooling of the lower layers at a higher pace compared to later layers along the build (z) direction and the pore distribution near the base plate follows the laser track pattern. A correlation between tensile properties and track overlap ratio was observed. The result reveals the maximum ultimate tensile stress (UTS) of 542.5 MPa was obtained at laser overlap of 30%, with a strain of 0.79. The sample fabricated with a 25% overlap exhibited a slightly reduced UTS of 529.6MPa and similar strain (0.74). By increasing overlap to 35%, UTS dropped significantly (458 MPa) but the sample is more ductile (strain is 0.97). Further increase overlap results in a slight increase of UTS and decrease of strain at UTS.

Overall, the neutron imaging and diffraction experiments nondestructively provide valuable material characterization for these DED produced samples. Probing the microstructural properties of these specimens helps to inform the fabrication process' impact on the final product, which in turn can be used to optimize the fabrication process to ultimately produce high-quality parts. This work has helped demonstrate the place of neutron imaging and diffraction in a multimodal nondestructive examination workflow for the inspection of AM components.

3.3 Lockin Thermography on 316L DED Specimens

In FY23, photothermal radiometry (PTR) measurements were conducted on LPBF manufactured SS tracks. PTR can measure local thermal diffusivity of the material, which is correlated to the microstructure information, such as porosity. PTR uses an intensity modulated laser to locally heat up the sample surface and monitors the induced local temperature variation from collecting the blackbody radiation. Development of an upgraded technique of PTR, namely LIT, was also initiated.

3.3.1 Development of LIT and multi-point LIT (MLIT)

In FY24 LIT development was completed. LIT shares similar physics to PTR, with the major difference between them being LIT's use of a million-pixel infrared (IR) camera to measure the temperature variation in an area of ~10mm*10mm instead of using a liquid-nitrogen cooled detector to measure the temperature variation point-by-point as in PTR. LIT significantly reduces the experiment time of PTR from 30-60 minutes to 10-30 seconds without sacrificing measurement accuracy. The optical system is also remarkably simplified, making LIT more feasible to be deployed into limited spaces.

LIT maintains all other advantages of PTR: measurements are remote and nondestructive; reasonable measurement accuracy can be obtained on industrial-grade rough surfaces; and measurement accuracy improves at elevated temperature (Hua 2022, Fabbri 1995). All these advantages make LIT a powerful tool to rapidly screen the thermal property and characterize microstructure of AM produced materials in operando and during the printing process. The microstructure induced thermal anisotropy in AM parts can also be revealed by LIT (Svetlizky 2021).

The LIT technology was further developed to create multi-point LIT, or MLIT. By using specific optics, a 5-by-5 matrix of laser spots with adjustable separation (approximately 2mm in the current setup) is generated to heat up the sample surface, and the temperature variation is captured by the camera. With synchronized laser intensity modulation, running a set of MLIT measurement is equivalent to simultaneously performing 25 LIT measurements. It provides the mapping capability to LIT and further improves the measurement efficiency. A journal publication summarizing the development of MLIT is under preparation and is expected to be finished by October 2024.

3.3.2 Application of LIT to AMMT-relevant samples

After validating MLIT on reference materials (pyrex, pyroceram, CaF2, Al2O3, and poco graphite, covering a wide thermal diffusivity range from ~1 mm2/s to ~70 mm2/s, and TiO2 that has an anisotropic thermal diffusivity), thermal diffusivity of a series of DED samples was mapped. These samples were printed with various manufacturing conditions. Mapping the thermal diffusivity, can provide a better understanding of how bulk porosity and local porosity variation are correlated to manufacturing parameters. One example of the thermal diffusivity mapping on the DED sample is given in Figure 38. The high porosity region at the bottom of the sample, revealed by the high-resolution image taken with a metallurgical microscope (left), is also captured by the thermal diffusivity mapping (middle and right).

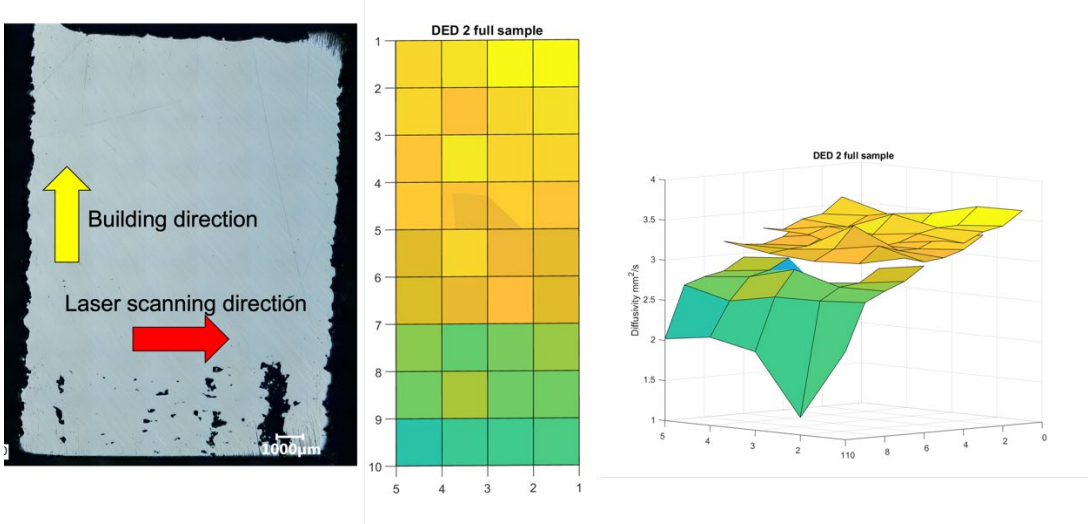

Figure 38. (Left) a picture of a DED sample, taken from a high-resolution metallurgical microscope. (Middle, Right) Thermal diffusivity mapping of the same DED sample, with high thermal diffusivity indicated by yellow and low thermal diffusivity by green. A clear correlation between a high porosity and low thermal diffusivity can be seen.

Data analysis indicates that the DED laser power is most importantly related to the formation of porosity, followed by the powder feed rate and laser scan velocity Additionally, the popularly used Global Energy Density (GED) has minimal impact on the formation of porosity (Ahn 2021). A more detailed quantitative analysis is ongoing. Both PTR and LIT measurements have the spatial resolution and profiling depth on the order of magnitude of mm (moderately adjustable by changing the modulation frequency of the heating laser in the range of ~0.1 mm to 2 mm). Comparing to the computed tomography techniques, this is still considered as a “surface measurement”.

MLIT was also applied to characterize the thermal diffusivity distribution of a functionally graded material (FGM) sample. This DED-produced FGM, shown in Figure 39, has three compositions: copper, nickel alloy (D22), and SS316L, from top to the bottom. Sixteen MLIT measurements were performed on the same sample at slightly different locations to improve the spatial resolution, with each measurement shifted a certain distance from the previous one. The final thermal diffusivity mapping, obtained through post-processing, clearly shows a reducing trend from the copper-rich region to the SS316L-rich region. The D22 and SS316L regions show similar thermal diffusivity and can hardly be differentiated. This is likely caused by the D22 region, which has a higher literature thermal diffusivity if 100% dense, and has higher porosity. Furthermore, the copper-rich region is expected to have a higher thermal diffusivity. The apparently lower thermal diffusivity is likely from the combined effects of high porosity and limited domain size. Thermal wave analytical models are known to underestimate thermal diffusivity if the semi-infinite assumption is violated (Hua 2022, Hua 2017). A numerical thermal transport model will be needed to correctly extract thermal diffusivity from a small volume sample.

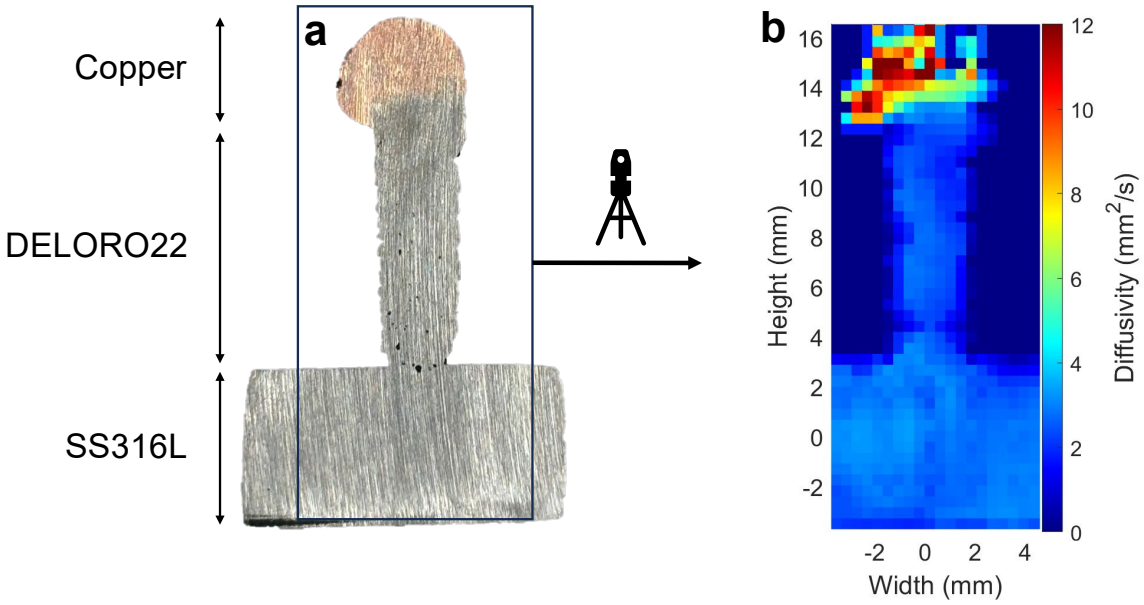

Figure 39. (a) The photo of the FGM sample, taken using a metallurgical microscope; (b) the thermal diffusivity mapping of the same FGM sample, with red indicating high thermal diffusivity and blue indicating low thermal diffusivity.

3.4 Positron Annihilation Spectroscopy

Positron annihilation spectroscopy (PAS) is a nondestructive technique that provides information on vacancies present in a material, including the early stages of detect formation as well as their evolution (Selim 2021, Siegel 1980). This technique works by utilizing a positron source (usually Na-22) to project positrons into a sample, where they annihilate with electrons in the sample, resulting in two characteristic twin 511 keV peaks. The lifetime of the positron, calculated from the original de-excitation of the Na-22 daughter to the detection of either 511 keV photon, is recorded. The measurement of many positron lifetimes can enable researchers to determine the size, quantity and form of material void space and defects. PAS measurements are often compared with other experimental techniques or electronic structure calculations to interpret the experimental data as it does not provide a direct link between signal and defect type (Wiktor 2016).

An extension of PAS is Coincidence Doppler Broadening PAS (CDB) where two detectors are configured in coincidence with one another to simultaneously measure the photon energy from the annihilation of a positron and electron. This technique utilizes the high energy resolution of the detectors to characterize the energy shift of the photons within the sample. As the two photons are emitted and traverse through the sample material in opposite directions, they are doppler shifted with one photon upshifting and the other downshifting. The local chemical environment within a sample can be ascertained from the element-specific spectral distributions corresponding to the momentum distributions of the annihilating electrons. Information on the local chemical environment where the positron annihilates is provided by the orbital electron momentum spectrum (OEMS) (Hu 2017).

3.4.1 Ex-situ experiment set up at INL

Figure 40 shows a bench top set up at the Materials and Fuels Complex in INL. Two scintillator BaF_2 detectors were set up for the PALS measurement while two high purity germanium (HPGe) detectors were set up for the CDB measurement (Figure 40). A digital PAS system by TechnoAP Co., Ltd. was used for data acquisition. Two identical samples are required for high quality measurements. Under circumstances when only one sample is available, a well characterized annealed backing material should be used to sufficiently block off all positrons. The NIST ESTAR program or ICRU Report 37 is referenced when sample thickness needs to be calculated (Berger 1999). A typical PAS measurement takes 24 hours for good statistics after source contribution subtraction. PAS data are fitted with PALSFIT or LT program, while the CDB data are analyzed using an INL developed program CDB-AP (Evans 2023).

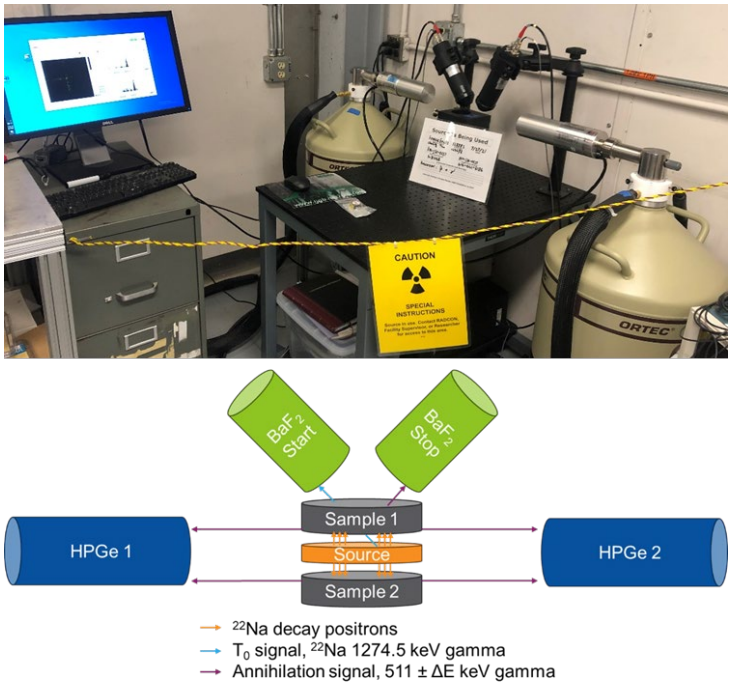

Figure 40. (top) Simultaneous PALS and CDB measurement set up. (bottom) Schematic of a PAS measurement with PALS and CDB modes using a 22Na positron source.

3.4.2 In-situ experimental concepts

External resources were leveraged to perform in-situ PAS at the Ohio State Research Reactor (OSURR). During these experiments, unirradiated and lightly irradiated DED SS316L specimens were measured with PAS. The goal of these experiments was to nondestructively observe defects in these samples to better understand the impact of AM fabrication processes on sample microstructure.

While the *ex-situ* studies mentioned above can provide information about defect density, size, and type, they are incapable of discovering defect dynamics. A previous Laboratory Directed Research and Development (LDRD) project proposed to leverage a neutron source for positron generation via high energy gamma pair production and for simultaneous irradiation both in the sample, to mitigate the complexity in post-irradiation sample handling and to minimize the loss of defect information during sample transfer. The principle of this approach is: a beam of

neutrons, regulated by a specially designed beam limiter, enters the chamber where the sample is located; the sample is irradiated by the neutron beam; the transmitted neutrons will cause (n,γ) reactions in the converting layers; the high energy γ rays will then generate positron-electron pairs inside the sample; the generated positrons will then annihilate with electrons in the sample and emit signals. The chamber wall consists of (n,γ) converting layers and neutron thermalization and reflecting layers. The aluminum outer wall is also designed to harden the gamma rays to reduce the low energy gammas that will interfere with the annihilation signal acquisition. The signals will be recorded by the well shielded detectors. The instrument sensitivity should provide detection of defects of close to 10^{-7} concentration and length scale on the order of angstroms. This technique is expected to provide defect concentration, size, and possibly type as functions of time and radiation dose. Figure 41 shows a schematic diagram of this set-up.

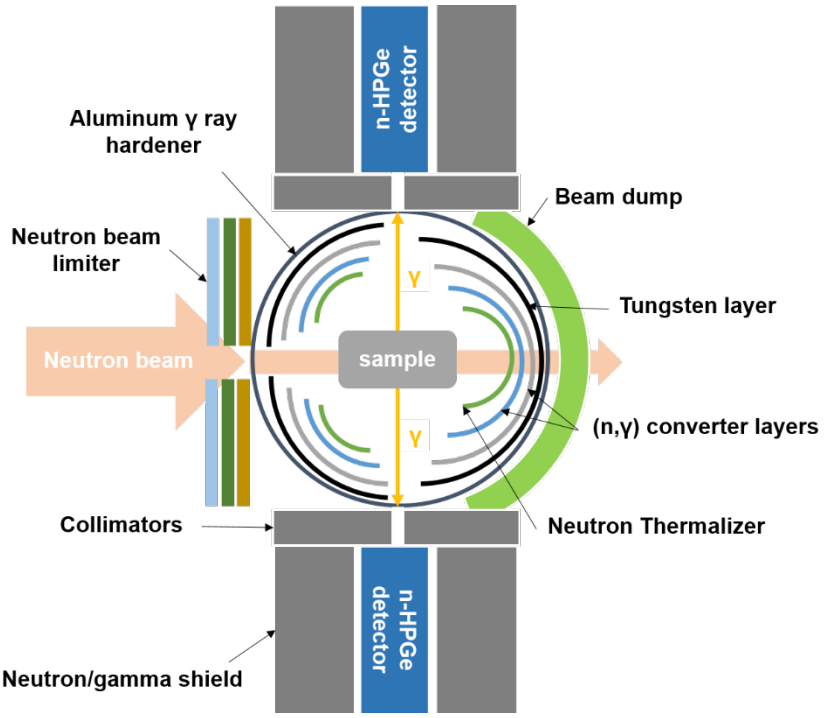

Figure 41. Preliminary design of the *in-situ* PAS experiment with simultaneous neutron irradiation.

This would be the very first time *in situ* PAS measurements are conducted with simultaneous neutron irradiation on any type of materials. The *in-situ* PAS is ideal for nuclear materials and fuels applications, as these materials are often of high Z (atomic number) elements, and pair production is proportional to Z^5. Additional advantages include but are not limited to (Selim 2017): 1) neutron damage and positron probing locations are coupled in real time; 2) early material damage can be detected dynamically while the damage is being created; 3) the positron signal is produced in the bulk volume; the sample can be of almost any shape or size and (almost) no special sample preparation is needed; 4) effects of sample matrix can be eliminated and risks associated with source safety can be mitigated; 5) samples can undergo extreme conditions of high temperature, pressure or stress and the PAS signals can still be collected. The measurements will be suitable for many applications, including low dose neutron irradiated steels and other alloys, for pressure vessels and fuel claddings; fuel samples; ceramic materials for variety uses, such as spent fuel storage; effects of hydrogen, helium and noble gas bubbles in metals; additively manufactured fuel and supporting components, etc.

The experiment was carried out at the Ohio State University Research Reactor's Fast Beam Facility (OSURR FBF) beam line (total neutron flux = $2.3x10^7$ nv (36% thermal)). The sample materials were cylinders of solid DED SS316L measuring 1.75" long x 0.5" diameter. Four such cylinders were fabricated using parameters in Table 16 and annealed to relieve machining stresses. Two of these samples were exposed to a reactor spectrum within the OSURR Central Irradiation Facility (CIF) before this experiment to induce 10^{-4} DPA and 10^{-5} DPA within the samples, respectively. Substantial work has been done in preparing for this experiment at the OSURR FBF including a full MCNP model of the experiment.

Table 16. DED Printing Parameters for the In-Situ PAS Experiment

Parameter	Value
Laser Power	250 W
Scan speed	8.5 mm/s
Powder feed-rate	14.4 g/min
Hatch distance	0.35 mm
Hatch angle	67
Anneal temp	1200 ºC
Anneal time	3 hrs
Anneal heating rate	10 ºC/min

3.4.3 Preliminary Results

Much of the effort of FY24 on in-situ PAS experiment went into assembling the experimental apparatus Figure 42 and Figure 43 highlight several stages of the assembly, 1) custom designed and fabricated tungsten collimator for shielding the detectors from excessive signal input and for capturing back-to-back coincidence Doppler shifts from the gamma spectrum, 2) modular experiment table with secured detector positions; and 3) removable sample chamber for sample change.

The experiment measured two samples, one annealed as fabricated sample, and one estimated 10^{-4} dpa sample. The same Techno-AP instrument from MFC was employed for data acquisition. In this experiment, positrons were created via pair-production from a flux of high energy photons *within* the sample, which themselves are produced from neutron capture and inelastic neutron scattering in and around the sample. The data was binned hourly; the change in the width of the 511 keV peak during each hour were expected to be used to infer a change in defect concentration within the sample.

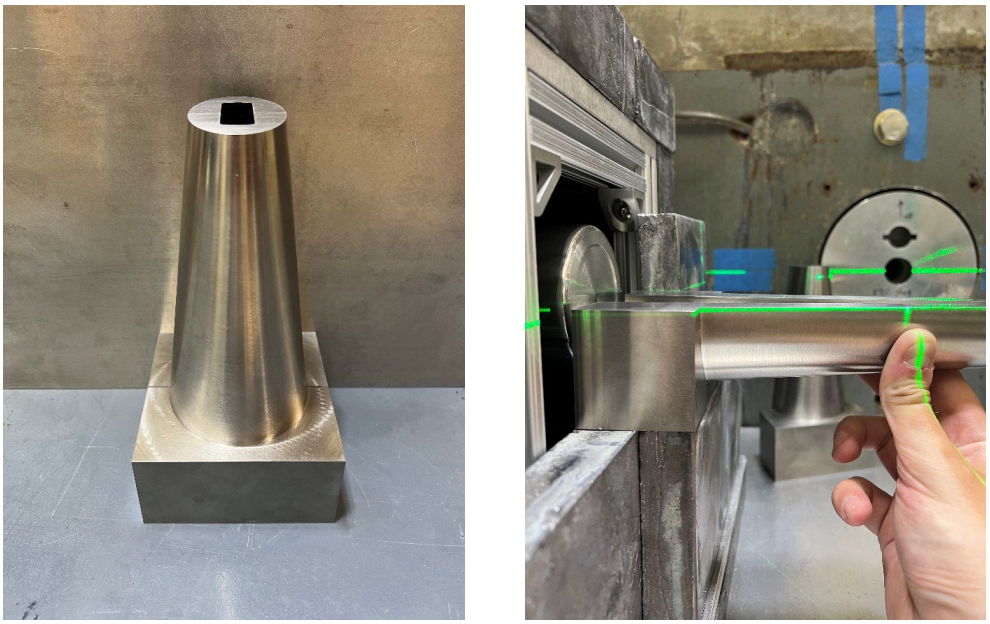

Figure 42. Custom Designed Tungsten Collimator.

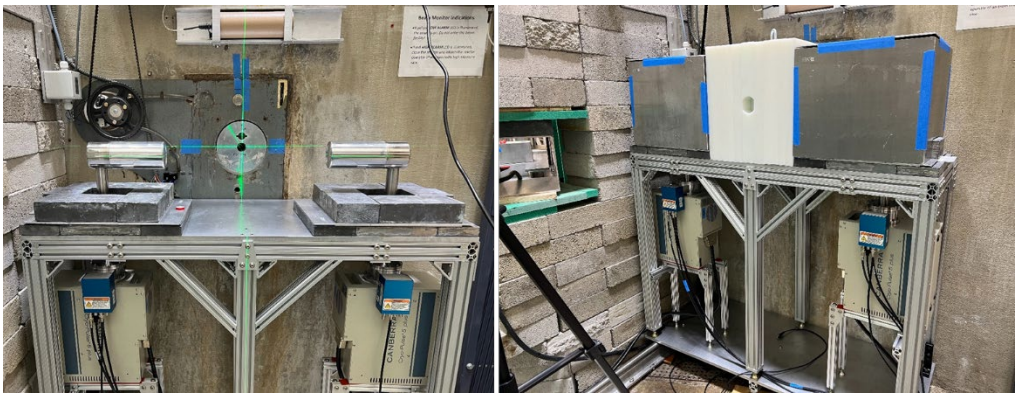

Figure 43. (Left) Laser aligned instrumentation at the OSURR FBF. (Right) Fully assembled experiment with sample inserted.

Initial experiments at OSURR were succesful as both high purity germanium (HPGE) detectors were able to resolve sharp 511 keV annihilation peaks (Figure 44). While the initial PAS measurement was successfully completed, this data is currently undergoing doppler broadening analysis to provide information on defects and void space within the samples. While successful, one of the detectors exhibited high deadtime and random noise, precluding coincidence measurements.

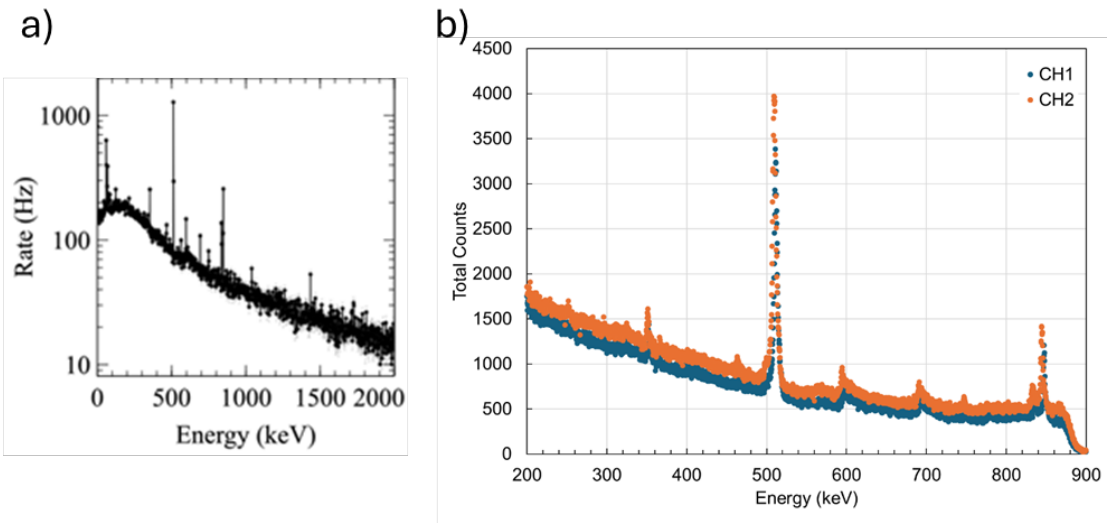

Figure 44. (a) MCNP Simulated Spectrum in One HPGe Detector and (b) Prominent 511 keV Signals in Both Detectors.

3.4.4 Future Work in PAS

Future work will involve doppler broadening of the data as well as coincidence measurements, which will both expand upon the preliminary characterization efforts. These successful OSURR experiments support an INL intern's PhD thesis in Applied Physics. Other notable FY24 outcomes include two conference presentations on the PAS work, including one invited talk to the *International Workshop on Positron Studies of Defects 2024*. As the PAS and CBD techniques are explored for additively manufactured materials, this work will introduce another nondestructive measurement tool in the multimodal workflow under development through this AMMT work package.

4.0 Observations and Recommendations

The AMMT program is accelerating the development, qualification, demonstration, and deployment of advanced materials and manufacturing technologies for advanced and current nuclear reactor systems (Li et. al., 2022). The development and use of post-process NDE methods is critical to the qualification and verification of materials and components from AM processes. The ability to perform reliable and accurate NDE will further drive the adoption of AM fabricated components for safety critical applications. Overcoming the unique challenges of AM components and materials (e.g., surface roughness, geometric complexity, microstructural features, and defect morphology) to provide reliable and high resolution NDE is the primary objective of the post-process NDE activities within the AMMT program.

The activities performed in FY24 to assess the post-process NDE characterization and inspection of materials and components fabricated using LPBF and DED processes made good progress in understanding the unique nature of these materials and how they interact with different NDE modalities. Exploring a spectrum of techniques that range in length scale from the angstrom level (PAS) to the engineering scale (e.g. XCT and ultrasonic testing) helps not only to demonstrate the usefulness of each technique in characterizing AM samples, but also helps lay the groundwork for a multi-modal, comprehensive characterization workflow. For example, the influence of LPBF fabrication on the anisotropic material behavior of both Alloy 709 austenitic stainless steel and Grade 92 ferritic/martensitic stainless steel was observed through UT methods. This information was used to correlate the anisotropic behavior to the fabrication process parameters. Understanding how the fabrication process can influence the material microstructure allows for adjustments and considerations to be incorporated in the methods to perform NDE inspections on AM components.

An important achievement this year was the multi-modal collaboration through complimentary examinations of the DED 316L coupons by XCT, LIT and UT approaches. Preliminary ultrasonic imaging and RUS analyses generated characterization results that were consistent with the XCT images and LIT evaluations obtained for the two DED 316L material coupons. The UT techniques were able to locate the porosity/defects within the coupons and provided estimates of the impact of these defects on the material elastic mechanical properties. This exercise provides an example of how complimentary examination techniques can facilitate the scale up of methods to qualify full size component inspections.

This work aligns with the AMMT objective to combine complementary destructive and nondestructive examination techniques across the critical length scales to create a feasible method for NDE of AM-produced nuclear reactor components during the build process, in the post-build condition, after installation, and during operational service. Such an approach will be needed as AM processes begin to fabricate larger and more complex components that are only inspectable with engineering-scale technologies. Figure 45 provides a schematic overview of the multi-scale and multi-modal approach to address the NDE challenges of materials and components fabricated with AM processes. This approach considers three different phases: Phase 1 – Material Characterization, Phase 2 – Subcomponent Testing, and Phase 3 – Component Examinations. Information and experience gained in one phase is used to support further evaluations in subsequent phases.

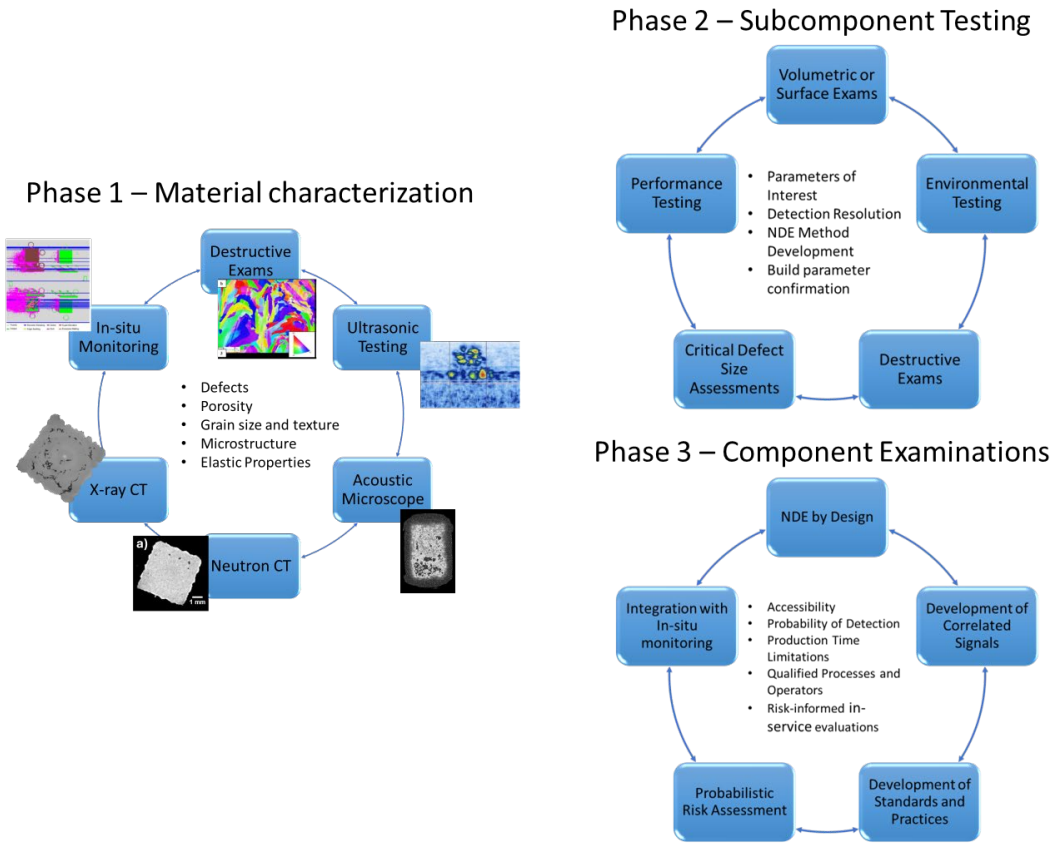

Figure 45. Multi-Modal and Multi-Scale Methodology to Develop Reliable and Accurate NDE Methods for Components Fabricated Using AM Processes

As highlighted in Phase 1, the material characterization efforts will generate the in-depth understanding of the relationships between build parameters, microstructure/properties, and defects and how the different NDE modalities detect and identify post-build conditions. From this work, correlations will arise between the different NDE results that can be scaled to larger volumetric inspections. The subcomponent testing in Phase 2 is the effort to establish the scale up to larger volume examinations combined with the environmental effects testing to identify the parameters of interest under service conditions and demonstrate the ability of NDE methods to provide appropriate detection resolution. Phase 3 concentrates on the challenges of applying post-build and in-service NDE to full-sized safety critical components, including accessibility, probabilistic considerations, and creation of qualified procedures and personnel.

The ability to correlate the detailed information coming from laboratory nondestructive and destructive examination techniques with the NDE methods applicable to production and operational conditions will increase the confidence in detecting material and component conditions important to assuring reliability and integrity.

The multi-modal and multi-scale development approach outlined above supports a new paradigm of NDE that will be required for qualification of AM parts for safety critical applications. The new NDE paradigm, shown in Figure 46, consists of printing witness coupons during a component build that can be inspected using destructive and nondestructive characterization methods to provide information on the material conditions produced by a build. This information is then used to confirm the final build state of the component using fast and inexpensive

validated volumetric inspection methods such as ultrasonic or eddy current NDE in key locations or subcomponent regions. These locations could be determined by probabilistic risk assessments performed to identify regions in the component susceptible to potential flaw nucleation and growth.

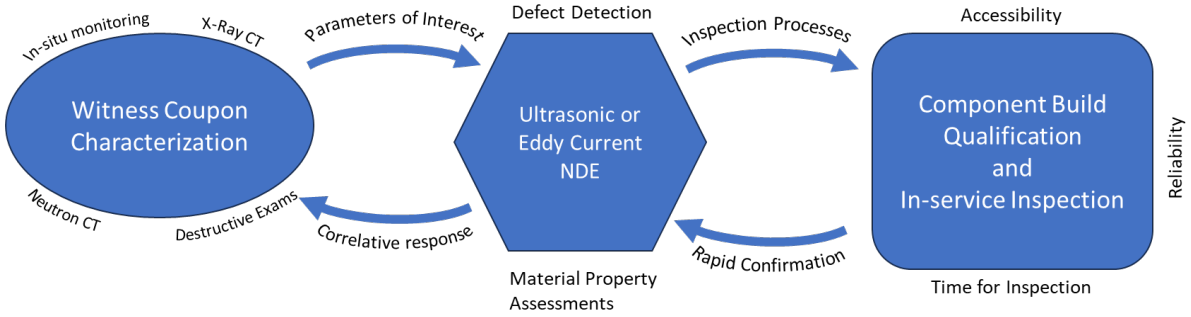

Figure 46. Post-Process NDE Paradigm for Qualification and In-Service Inspection of AM Components

Successful development of this NDE paradigm will require the data fusion of in-situ monitoring techniques to examine a part as it is built, post-process NDE to establish the final component state prior to service, and finally in-service NDE techniques that would monitor the integrity-critical areas during service. Such an approach would make for a more efficient and reliable examination effort that will establish the pedigree of the component throughout the lifetime, from the in-build condition to the end of the service life. By having baseline information on a component, it becomes possible to develop a relationship, i.e. chain of custody, between the AM processes for the component build parameters and the end of life condition. The application of this NDE paradigm is consistent with the use of the ASME XI Division 2 RIM requirements for advanced reactors. By developing a post-process NDE methodology for safety critical components fabricated with AM processes, the AMMT program is addressing an important hurdle to the industry and regulatory adoption of these advanced fabrication techniques.

The future efforts within the AMMT program will continue in the multi-modal and multi-scale collaboration initiative to build the methods and models that can scale information from coupons to full-size components. This will require additional experiments on AM samples to improve data collection efficiency as well as expand on the information that can be gained from these measurements. Further implementation and demonstration of data analytics and machine learning, such as the Simurgh algorithm for XCT reconstruction and algorithms for automated flaw detection and characterization, is also planned with the goal of increasing the throughput of examining AM parts by a variety of techniques. Lastly, correlations between techniques must be developed to enable multi-modal inferences to be derived from NDE measurements.

5.0 References

Ahn, D. G. (2021). Directed energy deposition (DED) process: state of the art. *International Journal of Precision Engineering and Manufacturing-Green Technology*, *8*(2), 703-742.

America Makes & ANSI Additive Manufacturing Standardization Collaborative (AMSC), (2023) Standardization Roadmap for Additive Manufacturing, Version 3.0, July 2023.

American Society of Mechanical Engineers, 2023 ASME Boiler & Pressure Vessel Code, Section XI, Division 2 Requirements for Reliability and Integrity Management (RIM) Programs for Nuclear Reactor Facilities, ASME Two Park Avenue, New York, 10016 USA.

Berger, M. J., Coursey, J. S., & Zucker, M. A. (1999). ESTAR, PSTAR, and ASTAR: computer programs for calculating stopping-power and range tables for electrons, protons, and helium ions (version 1.21).

Chuirazzi, W., Hua, Z., Tsai, C., Thompson, Z., and McMurtrey, M. “Nondestructive property and defect characterization using X-rays and neutrons.” INL/RPT-23-73813. (July, 2023).

Evans, G. S., Watkins, J. M., Taylor, C. N., Urban-Klaehn, J., & Tsai, C. T. (2023). CDB-AP: An application for coincidence Doppler broadening spectroscopy analysis. *SoftwareX*, *23*, 101475.

Fabbri, L., & Fenici, P. (1995). Three-dimensional photothermal radiometry for the determination of the thermal diffusivity of solids. *Review of scientific instruments*, *66*(6), 3593-3600.

Haines, N., Bell, J., and McIntyre, P., The Application of Broadband Ultrasonic Spectroscopy to the Study of Layer Media, J. Acoust. Soc. Am. 64, 1645–1651 (1978). https://doi.org/10.1121/1.382131.

Hasegawa, Y. (2014), 2 - Grade 92 creep-strength-enhanced ferritic steel, Coal Power Plant Materials and Life Assessment, Editor(s): Ahmed Shibli, Woodhead Publishing, Pages 52-86, ISBN 9780857094315, https://doi.org/10.1533/9780857097323.1.52.

Hu, X., Koyanagi, T., Katoh, Y., & Wirth, B. D. (2017). Positron annihilation spectroscopy investigation of vacancy defects in neutron-irradiated 3 C-SiC. *Physical Review B*, *95*(10), 104103.

Hua, Z., & Ban, H. (2017). Thermal diffusivity measurement of focused-ion-beam fabricated sample using photothermal reflectance technique. *Review of Scientific Instruments*, *88*(5).

Hua, Z., Schley, R., & Hurley, D. (2022). Local measurement of bulk thermal diffusivity using photothermal radiometry. *Review of Scientific Instruments*, *93*(4).

Jacob, R., et al. 2020, Survey of Pre-Service and In-Service Nondestructive Evaluation Techniques of AMT-Fabricated Components, PNNL-30759, United States Nuclear Regulatory Commission TLR-RES/DE/CIB-2020-12, ML20349A012.

Krautkrämer J. and Krautkrämer, H (1990) Ultrasonic Testing of Materials, Springer-Verlag, New York.

Lavrentyev, A and Rokhlin, S. (2001) An Ultrasonic Method for Determination of Elastic Moduli, Density, Attenuation and Thickness of a Polymer Coating on a Stiff Plate, Ultrasonics 39 (2001) 211-221.

Li, M., Andersson D., Dehoff, R., Jokisaari, A., Van Rooyen, I., and Cairns-Gallimore, D. 2022. Department of Energy Office of Nuclear Energy Advanced Materials and Manufacturing Technologies (AMMT) 2022 Roadmap, Report ANL-23/12, Argonne National Laboratory, Lemont, IL, https://www.energy.gov/sites/default/files/2023-03/ne-ammt-roadmap-030823.pdf.

Montgomery, R, Gillespie, J, Good, M, Chuirazzi W. Hua, Z., McMurtry M., I. 2023b. Initial Results of Post-Process NDE Using Advanced Techniques, PNNL-34855. United States Department of Energy M3CT-23PN1305092.

Montgomery, RO, Gillespie, JJ, Good, MS, Van Rooyen, I. 2023a. Comparison of Elastic Moduli of LPBF 316H Material Using RUS Measurements and Destructive Mechanical Testing, PNNL-34599. United States Department of Energy M3CT-23PN1305091.

Pang, J. H. L., Kaminski, J., & Pepin, H. (2019). Characterisation of porosity, density, and microstructure of directed energy deposited stainless steel AISI 316L. *Additive Manufacturing*, *25*, 286-296.

Reese, S.J., Smith, D.S., Rupp, R.E. et al. Elevated-Temperature Elastic Properties of Alloys 709 and 617 Measured by Laser Ultrasound. J. of Materi Eng and Perform 30, 1513–1520 (2021). https://doi.org/10.1007/s11665-020-05430-4.

Selim, F. (2017). Gamma induced positron annihilation: History, current, and future developments. *Acta Physica Polonica A*, *132*(5), 1450-1455.

Selim, F. A. (2021). Positron annihilation spectroscopy of defects in nuclear and irradiated materials-a review. *Materials Characterization*, *174*, 110952.

Siegel, R. W. (1980). Positron annihilation spectroscopy. *Annual Review of Materials Research*, *10*, 393-425.

Svetlizky, D., Das, M., Zheng, B., Vyatskikh, A. L., Bose, S., Bandyopadhyay, A., ... & Eliaz, N. (2021). Directed energy deposition (DED) additive manufacturing: Physical characteristics, defects, challenges and applications. *Materials Today*, *49*, 271-295.

Wiktor, J., Jomard, G., Torrent, M., & Bertolus, M. (2016). First-principles calculations of momentum distributions of annihilating electron–positron pairs in defects in UO2. *Journal of Physics: Condensed Matter*, *29*(3), 035503.

Zhang, X and Mantri, S, (2023) Evaluation of LPBF Steels for Nuclear Applications, Nuclear Science and Engineering Division, ANL-AMMT-006.

Ziabari, A., Venkatakrishnan, S., Dubey, A., Lisovich, A., Brackman, P., Frederick, C., ... & Paquit, V. (2022, October). Simurgh: A Framework for CAD-Driven Deep Learning Based X-Ray CT Reconstruction. In *2022 IEEE International Conference on Image Processing (ICIP)* (pp. 3836-3867). IEEE.

Pacific Northwest National Laboratory

902 Battelle Boulevard
P.O. Box 999
Richland, WA 99354

1-888-375-PNNL (7665)

www.pnnl.gov